DRAFT VERSION FEBRUARY 25, 2026
Typeset using LaTeX **twocolumn** style in AASTeX631

arXiv:2601.15142v2 [astro-ph.HE] 24 Feb 2026

Properties and Possible Physical Origins of γ-ray Emission in Extreme Synchrotron Blazars

JI-SHUN LIAN,[1] JIA-XUAN LI,[1] ZE-RUI WANG,[2] RUI-QI HUANG,[3] HAI-MING ZHANG†,[4] AND JIN ZHANG†[1]

[1]*School of Physics, Beijing Institute of Technology, Beijing 100081, People's Republic of China; j.zhang@bit.edu.cn*
[2]*College of Physics and Electronic Engineering, Qilu Normal University, Jinan 250200, People's Republic of China*
[3]*School of Physics, Beijing Institute of Technology, Beijing 100081, People's Republic of China*
[4]*Guangxi Key Laboratory for Relativistic Astrophysics, School of Physical Science and Technology, Guangxi University, Nanning 530004, People's Republic of China*

ABSTRACT

Extreme synchrotron blazars, characterized by a first peak in their broadband spectral energy distributions (SEDs) at frequencies exceeding 10^{17} Hz, often exhibit a second peak beyond 1 TeV. These sources serve as ideal laboratories for studying particle acceleration and radiation mechanisms in relativistic jets. In this work, we systematically analyze the $\sim$16-year Fermi-LAT observational data for 25 extreme high-synchrotron-peaked BL Lacs (EHBLs). The results indicate that the majority of these sources display stable or low flux levels in the GeV band, with only 6 sources showing significant variability at a confidence level exceeding 5σ. The time-averaged spectra over the 16-year period for most EHBLs are well described by a hard power-law model, with photon indices predominantly clustered between 1.7 and 1.8. Using Fermi-LAT data in conjunction with multiwavelength observations compiled from the literature, we construct broadband SEDs for these EHBLs and fit them with a one-zone synchrotron + synchrotron-self-Compton (SSC) model. We find that this simplified theoretical framework is sufficient for modeling the observed SEDs of most of these EHBLs, albeit requiring relatively higher electron energies compared to other γ-ray emitting HBLs, and at times under-representing the UV emission. Based on the SED fitting results, we investigate the physical properties of the emission regions in these EHBLs and compare them with those of other γ-ray emitting HBLs. Consistent with other GeV–TeV γ-ray-emitting BL Lacs, the jets in these EHBLs are marked by low radiation efficiency and low magnetization.

Keywords: gamma rays: galaxies – galaxies: blazars – galaxies: jets – radiation mechanisms: non-thermal

1. INTRODUCTION

Blazars are a subclass of active galactic nuclei (AGNs), characterized by relativistic jets oriented at small viewing angles (Blandford & Eichler 1987; Urry & Padovani 1995). They are further classified into Flat-spectrum radio quasars (FSRQs) and BL Lacertae objects (BL Lacs) based on the presence or absence of prominent optical emission lines (Stocke et al. 1991; Stickel et al. 1991; Fan 2003). The broadband spectral energy distributions (SEDs) of blazars, spanning from radio to γ-ray bands, are characterized by two humps and are dominated by the non-thermal emission from their relativistic jets, although thermal emission from the host galaxy, the accretion disk, and the dusty torus can lead to a more complex SED shape. The first hump is attributed to synchrotron radiation emitted by relativistic electrons within the jet, while the second hump is typically explained by inverse Compton scattering of low-energy photons by these same relativistic electrons. The seed photons for this scattering process may originate from the synchrotron radiation itself, a mechanism referred to as synchrotron self-Compton (SSC; e.g., Maraschi et al. 1992; Bloom & Marscher 1996; Mastichiadis & Kirk 1997; Zhang 2009; Zhang et al. 2012, 2014), or from external fields such as the accretion disk, broad-line region, or dusty torus, in which case it is referred to as external Compton (EC; e.g., Dermer et al. 1992; Sikora et al. 1994; Błażejowski et al. 2000; Ghisellini & Tavecchio 2009; Sikora et al. 2009; Zhang et al. 2014). Based on the peak frequency ($\nu_{\rm s,p}$) of the synchrotron emission, blazars are generally classified into three categories: low-synchrotron-peaked (LSP) blazars with $\nu_{\rm s,p} \leq 10^{14}$ Hz, intermediate-synchrotron-peaked (ISP) blazars with $10^{14} < \nu_{\rm s,p} < 10^{15}$ Hz, and high-synchrotron-peaked (HSP) blazars with $\nu_{\rm s,p} \geq 10^{15}$ Hz (Abdo et al. 2010; Fan et al. 2016; Singh et al.

Corresponding author: Jin Zhang
j.zhang@bit.edu.cn

2019; Acciari et al. 2020). FSRQs are almost exclusively LSP blazars (Giommi et al. 2012).

There also exists a small subset of BL Lacs that exhibit extremely high synchrotron-peaked (EHSP) behavior, with $\nu_{s,p} \geq 10^{17}$ Hz (Foffano et al. 2019). Moreover, the TeV-emitting EHSP BL Lacs (EHBLs) typically display a second spectral component peaking at ≥ 1 TeV in their SEDs (Singh et al. 2019; Biteau et al. 2020). These extreme peak characteristics in the broadband SEDs of BL Lacs can be observed both during flaring episodes and in quiescent states. These sources are characterized by hard spectra in both the soft X-ray and 0.1–1.0 TeV energy ranges, with photon spectral indices less than 2. For TeV-emitting BL Lacs, the one-zone synchrotron + SSC model is commonly employed to successfully reproduce their broadband SEDs (Tavecchio et al. 2010; Zhang et al. 2012). This model has also been applied to explain the broadband SEDs of EHBLs (e.g., Costamante et al. 2001a; Ghisellini et al. 2002; Bonnoli et al. 2015; Costamante et al. 2018; Acciari et al. 2020; Das et al. 2020; Tavecchio et al. 2022; Láinez et al. 2025). However, such modeling often requires extreme physical conditions within the emission region, such as a magnetic field strength significantly lower than the equipartition value (Tavecchio et al. 2010; Costamante et al. 2018; Sol & Zech 2022), an extremely hard electron spectrum (Biteau et al. 2020; Sol & Zech 2022; Goswami et al. 2024), a minimum electron Lorentz factor exceeding 10^3 (Tavecchio et al. 2010; Bonnoli et al. 2015; Cerruti et al. 2015; Aguilar-Ruiz et al. 2022), or a Doppler factor greater than 40 (Katarzyński et al. 2006; Cerruti et al. 2015; Costamante et al. 2018; Singh et al. 2019). These extreme BL Lacs offer a unique opportunity to investigate various high-energy astrophysical phenomena. They serve as ideal candidates for studying jet physics, particularly particle acceleration and radiation mechanisms, as well as for constraining models of the extragalactic background light (EBL) and the intergalactic magnetic field.

Variability across almost all energy bands, observed over different timescales ranging from a few minutes to several years, has been identified as a common characteristic of blazars (e.g., Albert et al. 2007a; Marscher et al. 2008; Padovani et al. 2017). Previous studies have shown that only a small fraction of HSP BL Lacs (HBLs) exhibit significant variability in the GeV γ-ray band, a proportion that is substantially lower than that observed in LSP BL Lacs (LBLs) and ISP BL Lacs (IBLs, Ackermann et al. 2011; Wang et al. 2024a). Most TeV-emitting BL Lacs also appear to remain stable over multi-year timescales in the TeV γ-ray band, although large statistical uncertainties prevent definitive conclusions regarding flux variations (Biteau et al. 2020). To date, Fermi-LAT has accumulated more than 17 years of observational data for these bright blazars, providing an opportunity to investigate their variability and radiation properties in the GeV band, as well as their flux states during TeV emission detections.

In this paper, we assemble a sample of TeV-emitting EHSP blazars, comprising 23 of the 24 sources listed in Table 1 of Biteau et al. (2020); RX J1136.5+6737 is excluded due to insufficient observational data. Additionally, two further sources, MRC 0910–208 and 1RXS J1958, are included based on their classification as EHBLs in the TeVCat catalog[1]. The final sample consists of 25 sources, all classified as EHBLs. We conduct a systematic analysis of the 16-year Fermi-LAT observational data for these sources to investigate their GeV γ-ray emission properties. Furthermore, we construct their broadband SEDs by combining the derived GeV-band spectra with archival data from the TeV and other wavelength bands, aiming to explore the underlying γ-ray radiation mechanisms. The methodology for Fermi-LAT data analysis is described in Section 2, and the corresponding results are presented in Section 3. The construction of SEDs and the results of model fitting are detailed in Section 4. Discussion and a summary are provided in Sections 5 and 6, respectively. Throughout, $H_0 = 71$ km s^{-1} Mpc^{-1}, $\Omega_m = 0.27$, and $\Omega_\Lambda = 0.73$ are adopted.

2. FERMI-LAT OBSERVATIONS AND DATA ANALYSIS

The PASS 8 data from the Fermi-LAT satellite within a 15° circular region of interest (ROI), centered on the radio positions of these EHBLs, were selected and downloaded from the Fermi Science Support Center[2]. The dataset spans from 2008 August 4 to 2024 September 22 (MJD 54682–60575), covering an energy range from 0.1 GeV to 1 TeV. The analysis was conducted using the publicly available software packages `fermitools` (version 2.2.0) and `Fermipy` (v1.1; Wood et al. 2017). Following the Fermi-LAT data selection recommendations[3], we employed event class "SOURCE" (evclass=128) and event type "FRONT+BACK" (evtype=3) for the binned likelihood analysis. To eliminate the contamination of γ-ray emission from the Earth's limb, we applied a zenith angle cut of less than 90°. The standard data quality filter "(DATA_QUAL>0)&&(LAT_CONFIG==1)" and the instrument response functions P8R3_SOURCE_V3 were used. The source model includes all γ-ray sources listed in the 4FGL-DR4 catalog (Abdollahi et al. 2020) within the ROI, as well as two background models: the isotropic emission model ("iso_P8R3_SOURCE_V3_V1.txt") and the galactic diffuse emission model ("gll_iem_v07.fits"). During the likelihood fitting process, only the parameters of sources located within 7.0° of the ROI center and the normalization

[1] http://tevcat2.uchicago.edu/

[2] https://fermi.gsfc.nasa.gov/cgi-bin/ssc/LAT/LATDataQuery.cgi

[3] https://fermi.gsfc.nasa.gov/ssc/data/analysis/documentation/Cicerone/Cicerone_Data_Exploration/Data_preparation.html

parameters of the two background models were allowed to vary; all other parameters were fixed to the values in the 4FGL-DR4.

For all sources in our sample, the spectral models recommended in the 4FGL-DR4 were consistently applied during data analysis. Specifically, the log-parabola (LP) model is

$$\frac{dN}{dE} = N_{\gamma,0}\left(\frac{E}{E_{\rm b}}\right)^{-\left(\Gamma_\gamma+\beta\log\left(\frac{E}{E_{\rm b}}\right)\right)}, \quad (1)$$

where $E_{\rm b}$ is the scale parameter of photon energy, Γ_γ is the photon spectral index, and β is the curvature parameter. If $\beta = 0$, the LP model turns into a power-law (PL) model,

$$\frac{dN}{dE} = N_{\gamma,0}\left(\frac{E}{E_{\rm b}}\right)^{-\Gamma_\gamma}. \quad (2)$$

For Mrk 421, a special function, PLSuperExpCutoff4, is required to describe its spectrum, which is structured as

$$\frac{dN}{dE} = \begin{cases} N_{\gamma,0}\left(\frac{E}{E_0}\right)^{-\Gamma_\gamma-\frac{\beta}{2}\ln\frac{E}{E_0}-\frac{\beta b}{6}\ln^2\frac{E}{E_0}-\frac{\beta b^2}{24}\ln^3\frac{E}{E_0}}, & \text{if } \left|b\ln\frac{E}{E_0}\right| < 1e^{-2}, \\ N_{\gamma,0}\left(\frac{E}{E_0}\right)^{-\Gamma_\gamma+\beta/b}\exp\left(\frac{\beta}{b^2}\left(1-\left(\frac{E}{E_0}\right)^b\right)\right) & \text{otherwise}, \end{cases} \quad (3)$$

where $N_{\gamma,0}$ is normalization (flux density) at E_0, E_0 is the scale parameter and β is the local curvature at E_0. E_0 and b are fixed at the value of 4FGL-DR4 as required, and Γ_γ is the photon spectral index.

We investigated potential new sources present in the ROI. The test statistic (TS) was utilized to evaluate the significance of a γ-ray source signal, where $\mathrm{TS} = 2(\log\mathscr{L}_{\rm src} - \log\mathscr{L}_{\rm null})$. Here, $\mathscr{L}_{\rm src}$ and $\mathscr{L}_{\rm null}$ denote the likelihood values of the background with and without the target source, respectively. A maximum TS value of $\geq$25 in the residual TS map indicates the detection of a new γ-ray source at the 5σ confidence level. We found a new γ-ray source located at (R.A.=166.20° $\pm$ 0.19°, Decl.=$-$24.85° $\pm$ 0.18°) with a TS = 34.1, which is 1.4° away from 1ES 1101–232. The flux of this new source is $(1.63 \pm 0.33) \times 10^{-12}$ erg cm^{-2} s^{-1} with a photon spectral index of $\Gamma_\gamma = 2.49 \pm 0.16$ in the 0.1–1000 GeV energy band. The presence of this newly identified source has been accounted for in the data analysis of 1ES 1101–232.

The long-term light curves were generated using the best-fit results, in which the normalization and spectral index of the target source were left free while all other sources within the ROI were kept fixed. The light curves were produced using the binned likelihood method with a time bin size of 90 days. A likelihood-based statistic was used to estimate the variability of the GeV light curves (e.g., Nolan et al. 2012; Peng et al. 2019; Abdollahi et al. 2020). Following the definition provided by Nolan et al. (2012), we calculated the variability index ($\mathrm{TS_{var}}$) as

$$\mathrm{TS_{var}} = 2\sum_{i=0}^{N}\left[\log\left(\mathscr{L}_i\left(F_i\right)\right) - \log\left(\mathscr{L}_i\left(F_{\rm global}\right)\right)\right], \quad (4)$$

where N represents the number of time bins of the light curves, F_i denotes the flux in the i-th bin, $F_{\rm glob}$ is the best fit flux over the entire time interval, and $\mathscr{L}_i(F_i)$ is the likelihood associated with the i-th bin. It should be noted that for a light curve comprising $N = 65$ time bins in this analysis, a value of $\mathrm{TS_{var}} \geq 138.8$ is required to identify a source as variable at the 5σ confidence level, corresponding to $N - 1 = 64$ degrees of freedom.

3. FERMI-LAT DATA ANALYSIS RESULTS

3.1. *Spectral Properties*

The 16-year Fermi-LAT average spectra for the 25 EHBLs in the 0.1–1000 GeV band, along with the corresponding fitting results, are presented in Figure 1. Among these, 18 spectra are well explained by a PL function, while 6 spectra require a curved LP model for an accurate fit; the only exceptional spectrum of Mrk 421 necessitates a more complex functional form for an appropriate representation. This is presumably because of the averaging over the 16-year observation data of this highly variable source, as Mrk 421 exhibits significant variability in both flux and spectrum. All sources display a hard spectra in the GeV band with $\Gamma_\gamma \leq 2.0$, as listed in Table 1. The Γ_γ values of these EHBLs range from 1.51 to 2.01, with a concentration between 1.70 and 1.80. The hardest and most curved spectrum is observed from RGB J0710+591, characterized by $\Gamma_\gamma = 1.51 \pm 0.08$ and $\beta = 0.060 \pm 0.026$. These hard GeV γ-ray spectra suggest the presence of a high-energy peak in the broadband SEDs of these sources. Additionally, we calculate the 16-year average flux in the 0.1–100 GeV band for the 25 EHBLs, which ranges from 1.20×10^{-12} erg cm^{-2} s^{-1} to 402.02×10^{-12} erg cm^{-2} s^{-1}, as detailed in Table 1. Mrk 421 displays the highest flux, exceeding the average flux of MRC 0910–208 by more than two orders of magnitude.

3.2. *Long-term Light curves*

Using the 16-year Fermi-LAT observation data, we generate the long-term γ-ray light curves of the 25 EHBLs in the 0.1–1000 GeV band with time bins of 90 days, as illustrated in Figure 1. Additionally, we compute $\mathrm{TS_{var}}$ values to quantify the variability of these sources, as summarized in Table 1. It is found that the majority of sources in the sample do not exhibit significant flux variability. According to the $\mathrm{TS_{var}}$ criterion, only six sources, namely Mrk 421, Mrk 501, 1ES 1218+304, 1ES 1712+502, 1ES 1959+650, and 1ES 2344+514, show variability at a confidence level exceeding 5σ. For several EHBLs, long-term γ-ray detections are either absent or sparse, with only upper limits reported in their light curves. In these cases, the number of detection points is substantially lower than the number of upper limits, including SHBL J001355.9–185406, 1ES 0229+200, 1ES 0347–121, PKS 0548–322, PGC 2402248, RBS 0723, 1ES 1440+122,

and 1ES 2037+521 (featuring fewer than 20 detection points in their respective light curves). These findings suggest that the emission of these EHBLs remains below the Fermi-LAT detection threshold over a period of three months.

In the long-term Fermi-LAT light curves, the time intervals corresponding to the TeV band observations used for SED modeling in Section 4 are indicated by pink shading, as illustrated in Figure 1. For sources whose TeV observations were conducted prior to the launch of the Fermi satellite, no such shaded regions appear in their Fermi-LAT light curves; these sources include 1ES 0347–121, PKS 0548–322, 1ES 1101–232, and 1ES 2356–309. As shown in Figure 1, the TeV detections of these EHBLs are generally not associated with a high-flux state in the GeV energy band.

4. SED CONSTRUCTION AND MODEL FITTING

4.1. *SED Construction*

The majority of these sources may exhibit EHBL characteristics only during flaring states and do not remain in the EHBL state continuously. For example, Mrk 421, Mrk 501, and 1ES 1959+650 are well-known HBLs that occasionally display extreme behavior (Ahnen et al. 2018; Foffano et al. 2019). In this study, we select only one broadband SED per source, with the condition that $\nu_{\rm s,p} \geq 10^{17}$ Hz. Except for the GeV spectra, multi-band data for the 25 EHBLs are compiled from existing literature; the highest flux state in the TeV band, together with the quasi-simultaneously observed multi-band data, is selected for each EHBL in cases where multiple observations are available. The broadband SEDs of the 25 EHBLs are presented in Figure 2, and detailed information regarding the data origins for each source refers to Appendix A.

The GeV spectra of these sources are obtained from the analysis results presented in this work and are selected according to the following criteria: (1) for the 19 sources exhibiting no significant variability, the 16-year averaged spectra are used; (2) for the six BL Lacs (Mrk 421, 1ES 1218+304, 1ES 1727+502, 1ES 1959+650, Mrk 501, and 1ES 2344+514) with significant variability, a reanalysis of Fermi-LAT observational data is conducted. Specifically, the contemporaneous Fermi-LAT spectra with the TeV observations are derived for Mrk 421, 1ES 1218+304, 1ES 1727+502, and 1ES 1959+650, i.e., their spectra in both GeV and TeV bands from the observation periods marked as the pink-shaded regions in their light curves in Figure 1. For the other two sources, Mrk 501 and 1ES 2344+514, the TeV spectra are from the observations within one day (the pink-shaded regions in their light curves in Figure 1), and no statistical signal can be obtained from the simultaneous Fermi-LAT observations. Therefore, slightly extended observation periods relative to the TeV campaigns are employed to ensure sufficient statistical significance of the GeV flux measurements, similar to the approach in MAGIC Collaboration et al. (2020a) and MAGIC Collaboration et al. (2020b). For Mrk 501, a 16-day period (the green-shaded region in its light curve in Figure 1) is selected to reanalyze the Fermi-LAT observational data, which corresponds to the MAGIC telescope observations during its very high energy flaring activity in July 2014 (MAGIC Collaboration et al. 2020a). The obtained GeV spectrum is consistent with the result of the MAGIC Collaboration using a 10-day time window centered on the very high energy observation time. For 1ES 2344+514, the same Fermi-LAT observation period as that in MAGIC Collaboration et al. (2020b) is chosen, that is, one month centered on the very high energy observation (the green-shaded region in its light curve in Figure 1). Details of the data reanalysis for the six sources are provided in Table 1.

4.2. *SED Fitting and Results*

To investigate the γ-ray emission mechanisms of these EHBLs, we employ the simplest theoretical framework, the one-zone leptonic synchrotron + SSC (one-zone SSC for short) model, to reproduce the broadband SEDs of the 25 selected EHBLs. This model is commonly used to explain the SEDs of TeV BL Lacs (Tavecchio et al. 2010; Zhang et al. 2012; Wang et al. 2024b; Láinez et al. 2025). The model calculations follow established computational methods (e.g., Rybicki & Lightman 1979; Katarzyński et al. 2001; Ghisellini 2013; Chen 2017), with detailed formulations provided in Appendix B. The spectral output of the model is determined by 9 parameters: the radius R, magnetic field strength B, and Doppler factor δ of the emission region; the broken power-law indices p_1 and p_2 of the electron energy distribution; the minimum ($\gamma_{\rm min}$), break ($\gamma_{\rm b}$), and maximum Lorentz factors ($\gamma_{\rm max}$) of the electrons; and the electron density parameter N_0. We assume $\delta = \Gamma$, where Γ denotes the bulk Lorentz factor of the emitting region.

Our strategy of SED fitting is to keep parameter values that are as consistent as possible with the parameter space reported for TeV BL Lacs in previous studies (e.g., Tavecchio et al. 2010; Zhang et al. 2012; Yan et al. 2014; Nievas Rosillo et al. 2022; Zhao et al. 2024). The constrained parameter ranges are as follows: $B \in [0.01, 1]$ G, $R \in [10^{16} - 10^{17}]$ cm, $\delta_{\rm D} \in [5 - 30]$, $p_1 \in [1.8 - 3]$, $p_2 \in [3.5 - 6]$, $\gamma_{\rm min} \in [1 - 10^4]$, $\gamma_{\rm b} \in [10^4 - 10^{6.5}]$, $\gamma_{\rm max} = 10 \times \gamma_{\rm b}$, and $N_0 \in [10^{-3} - 10^5]$ cm^{-3}. Given the numerous free parameters, the well-known intrinsic degeneracies among them, and the limited availability of broadband data that may be not strictly simultaneous, an adjustment "by eye" is still the most common approach for SED fitting (Sol & Zech 2022). We aim to identify a plausible set of model parameters that can reproduce the observed data, with main focus on the X-ray and γ-ray spectra. Therefore, the modeling results presented here do not represent an exhaustive exploration of all possible parameter

combinations or scenarios that could potentially fit the data within the framework of our model.

The fitting results are presented in Figure 2. Overall, the one-zone SSC model can well represent the broadband SEDs of these EHBLs. However, for several sources, the GeV spectra are not adequately described by this model. Specifically, RGB J0152+017, 1ES 0347–121, 1ES 0414+009, and 1ES 1741+196 exhibit relatively soft GeV spectra, leading to an excess at the low-energy end compared to model predictions. Additionally, the TeV spectra of four objects—TXS 0210+515, 1ES 0347–121, 1ES 0229+200, and 1ES 1101–232—show a hard spectrum in the very high energy band. These features suggest that a more complex model may be necessary to accurately describe their broadband SEDs, as the emission in the GeV–TeV energy range cannot be fully explained by a single SSC component.

The fitting parameter values for each SED are summarized in Table 2, and their distributions are shown in Figure 5. specifically, the magnetic field strength B ranges from 0.01 G to 0.6 G with a median of 0.07 G, while the Doppler factor varies between 5 and 30, with an average value of 14.6. The radii of the emission region are predominantly clustered within $10^{16} - 10^{17}$ cm. Our analysis indicates that the one-zone SSC model remains effective in reproducing the broadband SEDs of most EHBLs across the X-ray to TeV energy bands. However, this comes at the expense of (i) requiring relatively high values of N_0, $\gamma_{\rm min}$, and $\gamma_{\rm b}$ for certain sources, and (ii) failing to adequately account for simultaneous optical-UV data, which may originate from distinct emission components (e.g., Costamante et al. 2018; Biteau et al. 2020). A detailed comparison of these parameters with those reported for other HBLs is provided in Section 5.

The range of the synchrotron peaked frequency $\nu_{\rm s,p}$ is 1.0×10^{17} Hz $\leqslant \nu_{\rm s,p} \leqslant 9.7\times10^{18}$ Hz with a mean value of 1.0×10^{18} Hz, while the range of the SSC peaked frequency $\nu_{\rm c,p}$ is 9.8×10^{24} Hz $\leqslant \nu_{\rm c,p} \leqslant 1.2\times10^{27}$ Hz with a mean value of 1.7×10^{26} Hz.

4.3. *Jet Powers*

Based on the SED fitting parameters and following the method of previous works (e.g., Ghisellini et al. 2010; Zhang et al. 2012), we calculate the jet powers of the 25 EHBLs by assuming that the jets consist of electrons ($P_{\rm e}$), magnetic fields (P_B), and radiation ($P_{\rm r}$), i.e.,

$$P_{\rm jet} = \pi R^2 \Gamma^2 c\,(U_{\rm e} + U_B + U_{\rm r})\,, \tag{5}$$

$$U_{\rm e} = m_{\rm e} c^2 \int N(\gamma)\gamma d\gamma, \tag{6}$$

$$U_B = \frac{B^2}{8\pi}, \tag{7}$$

$$U_{\rm r} = \frac{L_{\rm bol}}{4\pi R^2 c \delta^4}, \tag{8}$$

where $L_{\rm bol}$ is the bolometric luminosity. The derived jet power and the powers of each jet component for these EHBLs are given in Table 4. We plot $P_{\rm r}$, $P_{\rm e}$, and P_B as a function of $P_{\rm jet}$ in Figure 3. For the majority of the sources, the jets exhibit low radiation efficiency and low magnetization, i.e., $P_{\rm r}/P_{\rm jet} < 0.1$ and $P_B/P_{\rm jet} < 0.1$.

5. DISCUSSION

To investigate the properties of these EHBL with respect to other HBLs, we perform a comparative analysis between the sample of 25 EHBLs and broader blazar populations. Based on Fermi-LAT data analysis results for these 25 EHBLs, we present a plot of Γ_γ versus L_γ in Figure 4, comparing them with a large sample of blazars from the 4FGL-DR3 catalog (Abdollahi et al. 2022). Here, L_γ refers to the luminosity in the 0.1–100 GeV energy band for both the 4FGL-DR3 catalog sources and the 25 EHBLs. The results show that these EHBLs are located within the HBL region of the $\Gamma_\gamma - L_\gamma$ parameter space and exhibit, on average, the hardest γ-ray spectra among all blazar subclasses. To assess whether the EHBLs differ statistically from typical HBLs in terms of L_γ, Γ_γ, and their joint distribution, we apply the Kolmogorov–Smirnov (K–S) test. This K–S test yields a probability value $p_{\rm KS}$; a two-dimensional K–S test result above 0.2 (or above 0.1 for one-dimensional tests) suggests strong evidence for no significant difference between the samples, whereas $p_{\rm KS} < 10^{-4}$ indicates strong evidence of a statistically significant difference. The computed $p_{\rm KS}$ values are approximately 1.3×10^{-6} for the L_γ distribution, 9.4×10^{-4} for the Γ_γ distribution, and 4.3×10^{-5} for the joint $L_\gamma - \Gamma_\gamma$ distribution. These results indicate that the distributions of L_γ and Γ_γ exhibit distinct differences between EHBLs and HBLs.

The distributions of the derived parameters by the SED fitting for these EHBLs are shown in Figure 5. For comparison, the parameter distributions of a HBL sample from Zhao et al. (2024) are also presented in Figure 5, where the broadband SEDs of HBLs are also modeled using the one-zone SSC framework. Although the parameter distributions of these EHBLs fall within the overall range observed for HBLs, we observe that, on average, EHBLs exhibit higher values of N_0, $\gamma_{\rm b}$, and $\gamma_{\rm max}$, and lower values of B and δ compared to HBLs. The elevated $\gamma_{\rm b}$ and $\gamma_{\rm max}$ values are necessary to account for the higher synchrotron peak energies characteristic of EHBLs. The median values of B and δ for these EHBLs are 0.06 G and 12, respectively, while the corresponding medians for HBLs are 0.06 G and 45. We further employ the K–S test to assess the statistical differences between the parameter distributions of EHBLs and HBLs; the resulting $p_{\rm KS}$ values are summarized in Table 3. The distributions of N_0, $\gamma_{\rm b}$, $\gamma_{\rm max}$, and δ are found to be significantly different between the two samples, while the B distribution

shows a marginal deviation. These results indicate that the one-zone SSC model remains applicable for describing the broadband SEDs of most these EHBLs, consistent with previous studies of some EHBLs by Tavecchio et al. (2010) and Zhang et al. (2012). Furthermore, extreme synchrotron sources may represent the high-energy tail of the blazar population (e.g., Ghisellini et al. 1998; Costamante et al. 2001a; Ghisellini et al. 2002; Biteau et al. 2020).

Based on the SED fitting parameters, we obtained the values of U_B and U_e for the emission regions of these EHBLs and plotted U_B against U_e in Figure 6. The corresponding data for HBLs from Zhao et al. (2024) are also included in the same figure. The 25 EHBLs lie within the distribution range of the HBL population. The K–S test comparing the $U_B - U_e$ relation between the EHBL and HBL samples yields $p_{KS} \sim 3.7 \times 10^{-4}$, suggesting statistical differences between the two populations. Consistent with the trend observed in HBLs, the majority of EHBLs exhibit $U_B < U_e$, indicating a deviation from the equipartition condition. However, all EHBLs have $U_B/U_e > 10^{-3}$, and on average, they display higher U_B/U_e ratios compared to HBLs. Using the Fermi-LAT observation data and the one-zone SSC model, Tavecchio et al. (2010) and Zhang et al. (2012) independently modeled the broadband SEDs of a TeV-emitting BL Lac sample, finding that most sources in their samples also show $U_B < U_e$. Furthermore, Nievas Rosillo et al. (2022) suggested that weakly magnetized jets are likely required for sources exhibiting strong TeV γ-ray emission, which is consistent with the characteristics of magnetically dominated FSRQ jets and particle-dominated GeV–TeV BL Lac jets (Zhang et al. 2014). Additionally, jets may not always be in equipartition between particles and magnetic fields (e.g., Lewis et al. 2018).

We further plotted P_r/P_{jet} versus P_B/P_{jet} in Figure 7, where P_r/P_{jet} and P_B/P_{jet} represent the radiation efficiency and the magnetization of the jets, respectively. The data for a GeV-TeV emitting BL Lac sample from Zhang et al. (2012) are also shown in Figure 7. It should be noted that approximately half of the sources overlap between the two samples; however, different SED data were used. for instance, for Mrk 421 and Mrk 501, data from the high-flux states were selected. On average, these EHBLs exhibit higher values of P_r/P_{jet} and P_B/P_{jet} compared to the GeV-TeV emitting BL Lacs in Zhang et al. (2012). Nevertheless, the majority of EHBL jets still display low radiation efficiency and magnetization, with both P_r/P_{jet} and P_B/P_{jet} below 0.1. The K–S test yields $p_{KS} \sim 0.21$ when comparing the $P_r/P_{jet} - P_B/P_{jet}$ distributions between the two samples, indicating no statistically significant difference.

6. SUMMARY

In this work, we systematically analyzed the 16-year Fermi-LAT observation data for a sample of 25 EHBLs. We constructed the broadband SEDs by combining the Fermi-LAT spectra with the TeV data, as well as other multiwavelength observations performed during the TeV campaigns from the literature. For the 19 objects that exhibited no significant variability in the GeV band, we utilized the Fermi-LAT spectra integrated over 16 years, while for the 6 sources with detected significant variability, we employed the Fermi-LAT spectra integrated over the same epoch as the TeV observations. With the caveat of data taken over very different timescales in different energy bands (from years to hours), we performed SED modeling using a one-zone SSC model. Based on the results of the Fermi-LAT data analysis and SED modeling, we conducted a comparative analysis with other γ-ray emitting HBL samples. The main findings can be summarized as follows.

- Most EHBLs exhibit a stable, or even low, flux in the GeV band, with only 6 out of 25 sources showing significant variability at a confidence level exceeding 5σ.
- The majority of the 25 EHBLs show a hard PL spectrum in the 0.1–100 GeV band, with photon spectral indices concentrated between 1.7 and 1.8.
- The one-zone SSC model remains adequate for describing the broadband SEDs of most EHBLs, requiring only relatively higher values of γ_b and γ_{max} compared to other γ-ray emitting HBLs.
- The derived emission region parameters from SED modeling are consistent with those of other γ-ray emitting HBLs, but sometimes fail to fully account for the UV flux, and instead indicate a deviation from the equipartition condition, with $U_B/U_e < 1$.
- Similar to other GeV-TeV γ-ray emitting BL Lacs, the jets in these EHBLs exhibit low radiation efficiency and magnetization.

ACKNOWLEDGEMENTS

We sincerely appreciate the anonymous referee for the helpful suggestions and valuable comments. This work is supported by the National Key R&D Program of China (grant 2023YFE0117200) and the National Natural Science Foundation of China (grants 12203024, 12203022, 12022305, 11973050, 12473042, and 12373109).

Table 1. Results from Fermi-LAT Observations of 25 EHBLs

Average Information								
Source	4FGL Name (4FGL)	z	Energy Flux♣ ($\times 10^{-12}$ erg cm^{-2} s^{-1})	Spectral Model	Γ_γ	β	TS	TS_{var}
SHBL J001355.9-185406	J0013.9-1854	0.095	2.87 ± 0.34	PL	1.87 ± 0.08	-	208	59.4
RGB J0152+017	J0152.6+0147	0.080	8.29 ± 0.46	PL	2.01 ± 0.04	-	949	106.9
TXS 0210+515	J0214.3+5145	0.049	5.85 ± 0.47	PL	1.88 ± 0.06	-	415	49.0
1ES 0229+200	J0232.8+2018	0.139	3.49 ± 0.41	PL	1.72 ± 0.07	-	234	31.0
1ES 0347-121	J0349.4-1159	0.188	4.79 ± 0.47	PL	1.77 ± 0.06	-	432	48.1
1ES 0414+009	J0416.9+0105	0.287	7.14 ± 0.54	PL	1.84 ± 0.05	-	561	68.4
PKS 0548-322	J0550.5-3216	0.069	3.24 ± 0.36	PL	1.79 ± 0.07	-	264	43.3
RGB J0710+591	J0710.4+5908	0.125	5.62 ± 1.02	LP	1.51 ± 0.08	0.060 ± 0.026	670	66.3
PGC 2402248	J0733.4-5152	0.065	2.63 ± 0.35	PL	1.72 ± 0.08	-	183	45.6
RBS 0723	J0847.2+1134	0.198	4.81 ± 0.44	PL	1.79 ± 0.06	-	414	64.2
MRC 0910-208	J0912.9-2102	0.198	1.20 ± 0.64	PL	1.80 ± 0.03	-	1298	44.6
1ES 1101-232	J1103.6-2329	0.186	5.59 ± 0.49	PL	1.71 ± 0.06	-	483	38.9
Mrk 421	J1104.4+3812	0.031	402.02 ± 4.37	PLSuperExpCutoff4	1.74 ± 0.003	0.009 ± 0.001	227937	3476.4
1ES 1218+304	J1221.3+3010	0.182	46.49 ± 2.19	LP	1.68 ± 0.02	0.023 ± 0.006	8627	286.9
1ES 1312-423	J1315.0-4236	0.105	6.08 ± 0.52	PL	1.78 ± 0.06	-	412	66.8
1ES 1426+428	J1428.5+4240	0.129	8.41 ± 0.55	PL	1.62 ± 0.03	-	1325	81.3
1ES 1440+122	J1442.7+1200	0.163	5.65 ± 0.45	PL	1.78 ± 0.05	-	512	73.5
Mrk 501	J1653.8+3945	0.034	117.30 ± 2.92	LP	1.75 ± 0.01	0.021 ± 0.003	48673	959.5
1ES 1727+502	J1728.3+5013	0.055	18.29 ± 1.33	LP	1.76 ± 0.03	0.016 ± 0.010	4006	312.2
1ES 1741+196	J1744.0+1935	0.084	9.37 ± 0.50	PL	1.97 ± 0.04	-	897	86.5
1RXS J195815.6-301119	J1958.3-3010	0.119	11.72 ± 0.68	PL	1.83 ± 0.04	-	854	69.7
1ES 1959+650	J2000.0+6508	0.047	106.94 ± 2.49	LP	1.76 ± 0.01	0.023 ± 0.003	38216	2223.4
1ES 2037+521	J2039.5+5218	0.053	5.42 ± 0.51	PL	1.78 ± 0.06	-	298	58.8
1ES 2344+514	J2347.0+5141	0.044	28.99 ± 1.69	LP	1.74 ± 0.02	0.042 ± 0.009	5155	217.7
H 2356-309	J2359.0-3038	0.165	5.14 ± 0.43	PL	1.81 ± 0.05	-	529	60.1

Results from Fermi-LAT Observations during TeV Observations ♦						
Source	4FGL Name	Time (MJD)	Energy Flux ($\times 10^{-12}$ erg cm^{-2} s^{-1})	Spectral Model	Γ_γ	TS
Mrk 421	4FGL J1104.4+3812	55237.0–55250.0	773.96 ± 124.70	PL	1.58 ± 0.05	905.7
Mrk 501	4FGL J1653.8+3945	56854.0–56870.0	$187.84.40 \pm 52.09$	PL	1.74 ± 0.10	160.7
1ES 1218+304	4FGL J1221.3+3010	54801.0–54983.0	46.29 ± 10.03	PL	1.69 ± 0.07	310.1
1ES 1727+502	4FGL J1728.3+5013	57306.0–57328.0	41.67 ± 17.65	PL	1.91 ± 0.21	40.3
1ES 1959+650	4FGL J2000.0+6508	57552.0–57554.0	605.33 ± 253.89	PL	1.70 ± 0.15	110.8
1ES 2344+514	4FGL J2347.0+5141	57596.5–57626.5	46.88 ± 9.52	PL	2.02 ± 0.19	46.4

♣Within the 0.1–100 GeV band.

♦For the six BL Lacs exhibiting significant variability, a reanalysis of Fermi-LAT observational data was conducted. The contemporaneous Fermi-LAT spectra with the TeV observations have been derived for Mrk 421, 1ES 1218+304, 1ES 1727+502, and 1ES 1959+650, which are associated with the observation periods marked as the pink-shaded regions in their light curves in Figure 1. For Mrk 501, a 16-day period (the green-shaded region in its light curve in Figure 1) was selected for the reanalysis of the Fermi-LAT observational data, and its TeV spectrum (presented in Figure 2) was obtained from the observation within MJD 56857 (the pink-shaded region in its light curve in Figure 1). For 1ES 2344+514, a one-month Fermi-LAT observation period (the green-shaded region in its light curve in Figure 1) centered on the very high energy observation (MJD 57611, the pink-shaded region in its light curve in Figure 1) was chosen. More details can be found in Section 4.1.

Table 2. SED Fitting Results for the 25 EHBLs

source	$N_0[\mathrm{cm}^{-3}]$	p_1	p_2	γ_{min}	γ_{b}	γ_{max}	δ	B [G]	R [cm]	U_B/U_{e}	Reference♦
SHBL J001355.9-185406	3E3	2.3	3.8	1	2.5E5	2.5E6	12	0.09	2.8E16	4.0E-2	(1)
RGB J0152+017	9.5E3	2.25	5	1	4E5	4E6	10	0.045	2.4E16	2.7E-3	(2–3)
TXS 0210+515	1E5	2.5	4	1	6E5	6E6	10	0.15	1E16	5.5E-3	(4)
1ES 0229+200	7.5E2	2.1	4	1E3	1.5E6	1.5E7	30	0.01	2.5E16	2.4E-3	(5)
1ES 0347-121	4E3	2.35	3.7	9E3	4E5	4E6	20	0.04	6E16	2.1E-1	(6–8)
1ES 0414+009	3E4	2.6	4.5	3E3	2E5	2E6	20	0.1	6.5E16	1.3	(9)
PKS 0548-322	2E2	2.1	4.5	2E1	6E5	6E6	7	0.1	5E16	5.0E-1	(10)
RGB J0710+591	8E2	2.2	3.5	2E3	5.7E5	5.7E6	30	0.03	3.1E16	6.9E-2	(11)
PGC 2402248	5E3	2.3	4.1	1E2	6E5	6E6	13	0.08	1.6E16	7.9E-2	(12–13)
RBS 0723	1E4	2.3	3.5	2E3	6E5	6E6	20	0.05	2.2E16	4.2E-2	(4)
MRC 0910-208	7E4	2.6	6	2E3	4.5E5	4.5E6	10	0.06	8.5E16	1.5E-1	(14)
1ES 1101-232	5E2	2.1	5	7E2	2E5	2E6	12	0.6	2.1E16	1.5E-1	(15)
Mrk 421	1E2	2	4	1.5E3	8.5E5	8.5E6	22	0.01	1E17	7.1E-3	(16–19)
1ES 1218+304	3E4	2.5	4.2	1E3	7E5	7E6	20	0.02	7.8E16	1.1E-2	(20–26)
1ES 1312-423	2E2	2.1	4	4E2	5.5E5	5.5E6	5	0.1	9.8E16	5.2E-1	(27)
1ES 1426+428	5E2	2.2	3.2	9E2	4E5	4E6	12	0.1	6E16	1.0	(4)
1ES 1440+122	4.8E2	2.15	4	1	5E5	5E6	5	0.11	1E17	2.1E-1	(28)
Mrk 501	1E3	2.2	5	1	3E6	3E7	6	0.08	9E16	6.5E-2	(29)
1ES 1727+502	7E3	2.4	5	7E2	1.2E6	1.2E7	12	0.02	8.5E16	1.6E-2	(30)
1ES 1741+196	5E4	2.5	4	1	4E5	4E6	6	0.2	3.2E16	1.9E-2	(31–32)
1RXS J195815.6-301119	4.5E4	2.5	3.5	6E2	4E5	4E6	6	0.14	5E16	2.7E-1	(14)
1ES 1959+650	6.8E3	2.3	3.5	4E2	7.8E5	7.8E6	11	0.05	6.5E16	3.5E-2	(30)
1ES 2037+521	2.3E4	2.5	4	5E2	9E5	9E6	30	0.01	2.3E16	2.4E-3	(33)
1ES 2344+514	1.8E4	2.4	3.5	3E2	1E6	1E7	18	0.01	4E16	1.1E-3	(34)
H 2356-309	1E3	2.3	3.5	2E3	3.2E5	3.2E6	18	0.02	1E17	6.9E-2	(35–36)

♦The references for the broadband SED data in Figure 2: (1) H. E. S. S. Collaboration et al. (2013); (2) Aharonian et al. (2008); (3) Nilsson et al. (2003); (4) Acciari et al. (2020); (5) Aliu et al. (2014a); (6) Tanaka et al. (2014); (7) Aharonian et al. (2007a); (8) Baumgartner et al. (2013); (9) H. E. S. S. Collaboration et al. (2012); (10) Aharonian et al. (2010); (11) Acciari et al. (2010a); (12) Medina-Carrillo et al. (2023); (13) MAGIC Collaboration et al. (2019); (14) Bony (de) et al. (2022); (15) Aharonian et al. (2007b); (16) Dmytriiev et al. (2021); (17) Banerjee et al. (2019); (18) Shukla et al. (2012); (19) Fortson et al. (2012); (20) Acciari et al. (2010b); (21) Rüger et al. (2010); (22) Acciari et al. (2009); (23) Albert et al. (2006); (24) Tramacere et al. (2007); (25) Donato et al. (2005); (26) Chen et al. (2005); (27) HESS Collaboration et al. (2013); (28) Archambault et al. (2016); (29) MAGIC Collaboration et al. (2020a); (30) MAGIC Collaboration et al. (2020c); (31) Abeysekara et al. (2016); (32) Ahnen et al. (2017); (33) Prandini & MAGIC Collaboration (2019); (34) MAGIC Collaboration et al. (2020b); (35) H. E. S. S. Collaboration et al. (2010); (36) Costamante et al. (2001a).

Table 3. Results of the K–S Test

Figure	Parameters	$p_{\rm KS}$
Fig.4	L_γ	1.3×10^{-6}
	Γ_γ	9.4×10^{-4}
	$L_\gamma-\Gamma_\gamma$	4.3×10^{-5}
Fig.5	N_0	8.8×10^{-12}
	p_1	1.3×10^{-3}
	p_2	8.5×10^{-6}
	$\gamma_{\rm min}$	2.3×10^{-4}
	$\gamma_{\rm b}$	3.7×10^{-19}
	$\gamma_{\rm max}$	3.0×10^{-11}
	B	2.8×10^{-2}
	δ	1.6×10^{-12}
	R	1.3×10^{-5}
Fig.6	$U_B-U_{\rm e}$	3.7×10^{-4}
Fig.7	$P_{\rm r}/P_{\rm jet}-P_B/P_{\rm jet}$	2.1×10^{-1}

Table 4. Derived Parameters from SED Fitting for the 25 EHBLs

Object	$P_{\rm jet}$ [erg s^{-1}]	$P_{\rm r}$ [erg s^{-1}]	$P_{\rm e}$ [erg s^{-1}]	P_B [erg s^{-1}]	$\nu_{\rm s,p}$ [Hz]	$L_{\rm s,p}$ [erg s^{-1}]	$\nu_{\rm c,p}$ [Hz]	$L_{\rm c,p}$ [erg s^{-1}]
SHBL J001355.9-185406	8.98E43	1.49E42	8.49E43	3.43E42	2.00E17	1.10E44	4.36E25	1.74E43
RGB J0152+017	1.64E44	1.68E42	1.62E44	4.37E41	1.48E17	6.09E43	5.88E25	4.78E43
TXS 0210+515	1.54E44	7.02E41	1.53E44	8.43E41	1.20E18	2.94E43	3.24E25	6.10E42
1ES 0229+200	8.96E43	1.13E42	8.83E43	2.11E41	2.17E18	5.35E44	1.16E27	1.65E44
1ES 0347-121	5.81E43	8.27E42	4.12E43	8.63E42	3.63E17	1.65E45	1.53E26	4.28E44
1ES 0414+009	1.29E44	1.54E43	4.99E43	6.33E43	1.04E17	2.90E45	1.78E25	6.18E44
PKS 0548-322	1.80E43	4.18E42	9.19E42	4.59E42	6.60E17	1.39E44	1.07E26	1.24E43
RGB J0710+591	4.73E43	2.52E42	4.18E43	2.92E42	1.20E18	1.22E45	3.73E26	1.66E44
PGC 2402248	1.48E43	7.01E41	1.30E43	1.04E42	1.13E18	6.58E43	1.07E26	7.83E42
RBS 0723	5.00E43	4.86E42	4.33E43	1.81E42	1.52E18	8.34E44	2.06E26	3.03E44
MRC 0910-208	8.85E43	1.34E43	6.54E43	9.75E42	1.40E17	4.47E44	9.82E24	3.01E44
1ES 1101-232	1.18E44	2.69E43	5.72E42	8.57E43	6.21E17	2.82E45	4.36E25	1.90E44
Mrk 421	2.70E44	1.39E43	2.55E44	1.81E42	6.21E17	3.05E45	6.38E26	1.84E45
1ES 1218+304	3.58E44	1.07E43	3.44E44	3.65E42	3.63E17	1.26E45	6.24E25	9.73E44
1ES 1312-423	3.82E43	1.83E43	1.09E43	9.00E42	4.90E17	2.69E44	6.24E25	4.82E43
1ES 1426+428	5.64E43	1.77E43	1.92E43	1.94E43	1.20E18	1.32E45	1.44E26	1.48E44
1ES 1440+122	9.49E44	3.00E43	5.36E43	1.13E43	4.61E17	3.96E44	4.36E25	1.02E44
Mrk 501	1.74E44	6.07E43	1.07E44	6.99E42	9.65E18	1.30E45	2.77E26	2.40E44
1ES 1727+502	1.03E44	4.03E42	9.73E43	1.56E42	6.60E17	2.39E44	1.07E26	1.06E44
1ES 1741+196	2.94E44	6.79E42	2.82E44	5.53E42	4.61E17	9.13E43	1.32E25	3.09E43
1RXS J195815.6-301119	4.53E43	1.39E43	2.47E43	6.61E42	4.61E17	1.64E44	1.78E25	8.42E43
1ES 1959+650	1.80E44	3.98E43	1.35E44	4.79E42	1.52E18	1.61E45	1.44E26	1.09E45
1ES 2037+521	8.75E43	1.21E41	8.72E43	2.11E41	6.21E17	4.65E43	1.44E26	9.90E42
1ES 2344+514	1.79E44	8.73E41	1.78E44	1.94E41	6.60E17	8.63E43	2.06E26	5.81E43
H 2356-309	7.84E43	3.58E42	7.00E43	4.86E42	1.40E17	5.31E44	1.07E26	1.51E44

Fig. Set 1. The ∼16-year Fermi-LAT average spectra and the long-term light curves in the 0.1–1000 GeV band for the 25 EHBLs.

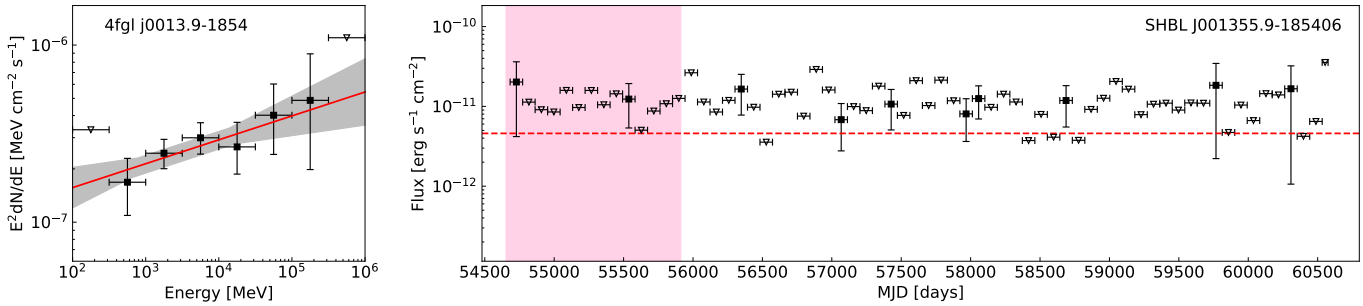

Figure 1. Left column: the ∼16-yr Fermi-LAT average spectra along with the fitting results, where the open inverted triangles indicate TS<4 for that energy bin. Right column: the long-term Fermi-LAT light curves with time bins of 90 days, where the open inverted triangles indicate the TS value of that time bin less than 9. The horizontal red dash lines represent the ∼16 yr average γ-ray flux of the sources. The pink-shaded regions denote the period covered by the TeV observations, as well as other multiwavelength observations performed during the TeV campaigns. For sources such as 1ES 0347–121, PKS 0548–322, 1ES 1101–232, and 1ES 2356–309, whose TeV observations were conducted prior to the launch of the Fermi satellite, no such shaded regions appear in their Fermi-LAT light curves. For the four BL Lacs (Mrk 421, 1ES 1218+304, 1ES 1727+502 and 1ES 1959+650; marked with a red star in the light-curve figure panels) with significant variability, the contemporaneous Fermi-LAT spectra with the TeV observations are derived to construct their broadband SEDs in Figure 2, that is, their spectra in both the GeV and TeV bands from the observation periods marked as the pink-shaded regions in their light curves. For the other two sources (Mrk 501 and 1ES 2344+514, marked with a red rhombus in the light-curve figure panels) with significant variability, slightly extended observation periods (the green-shaded regions in their light curves) relative to their TeV campaigns (the pink-shaded regions in their light curves) are employed to generate the GeV spectrum for their broadband SED construction. For the remaining 19 objects, the 16-year Fermi-LAT averaged spectra are used to construct their broadband SEDs in Figure 2.

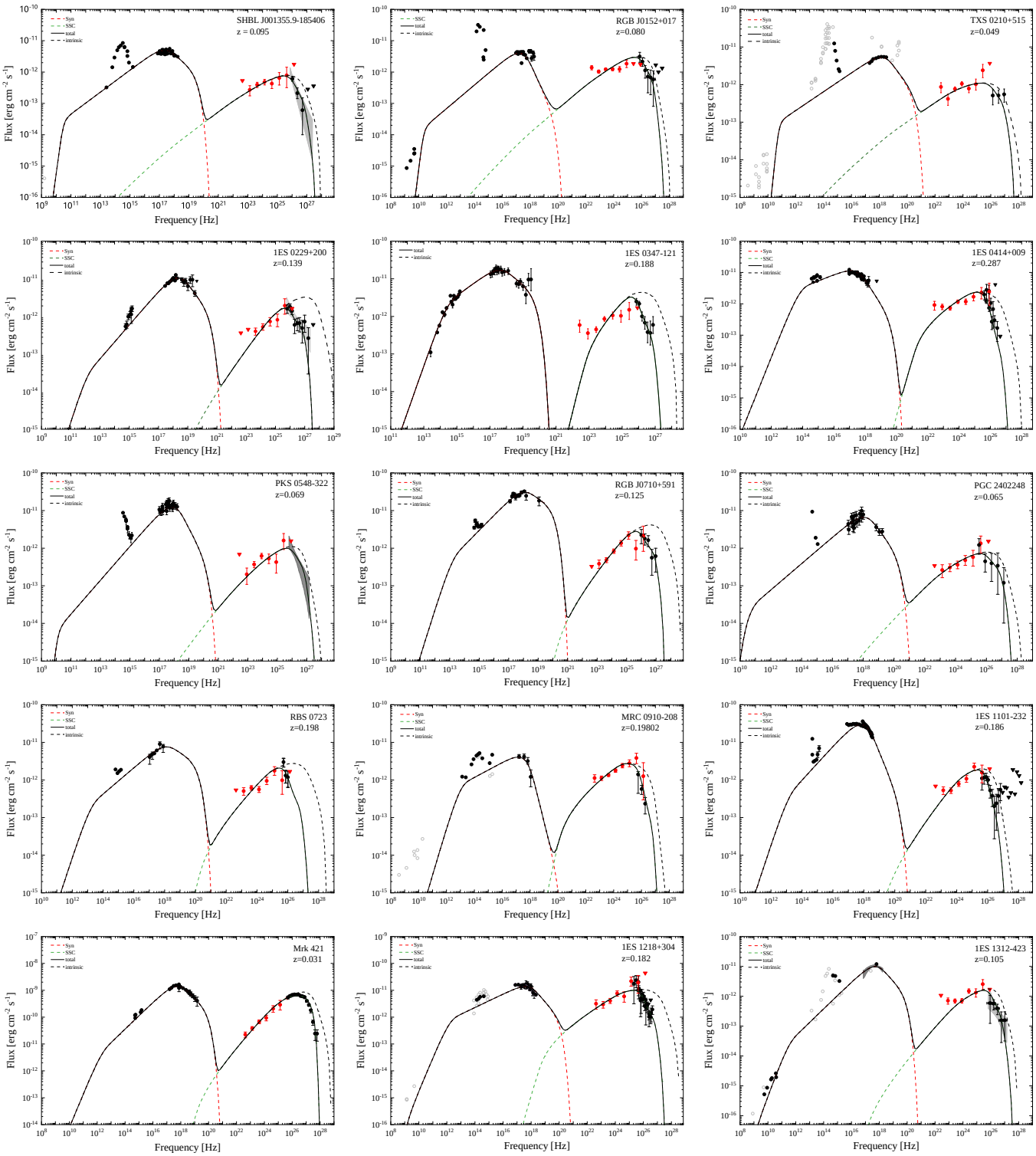

Figure 2. Observed SEDs (scattered data points) with the one-zone SSC model fits (lines) for the 25 EHBLs. The red solid circles and inverted triangles represent Fermi-LAT data obtained in this study. Black solid circles and inverted triangles denote the simultaneous or quasi-simultaneous observation data from the previous works (see Table 2 and Appendix A for details on each source), along with the archived data (gray hollow dots). Inverted triangles denote upper limits. The TeV γ-ray data have been corrected to the observer's frame using the EBL model in Finke et al. (2022). The black solid lines represent the total modeled flux, comprising the sum of the synchrotron radiation component (red dashed line) and the SSC contribution (green dashed line). The black dashed lines in the TeV energy range show the intrinsic model-predicted fluxes before EBL absorption.

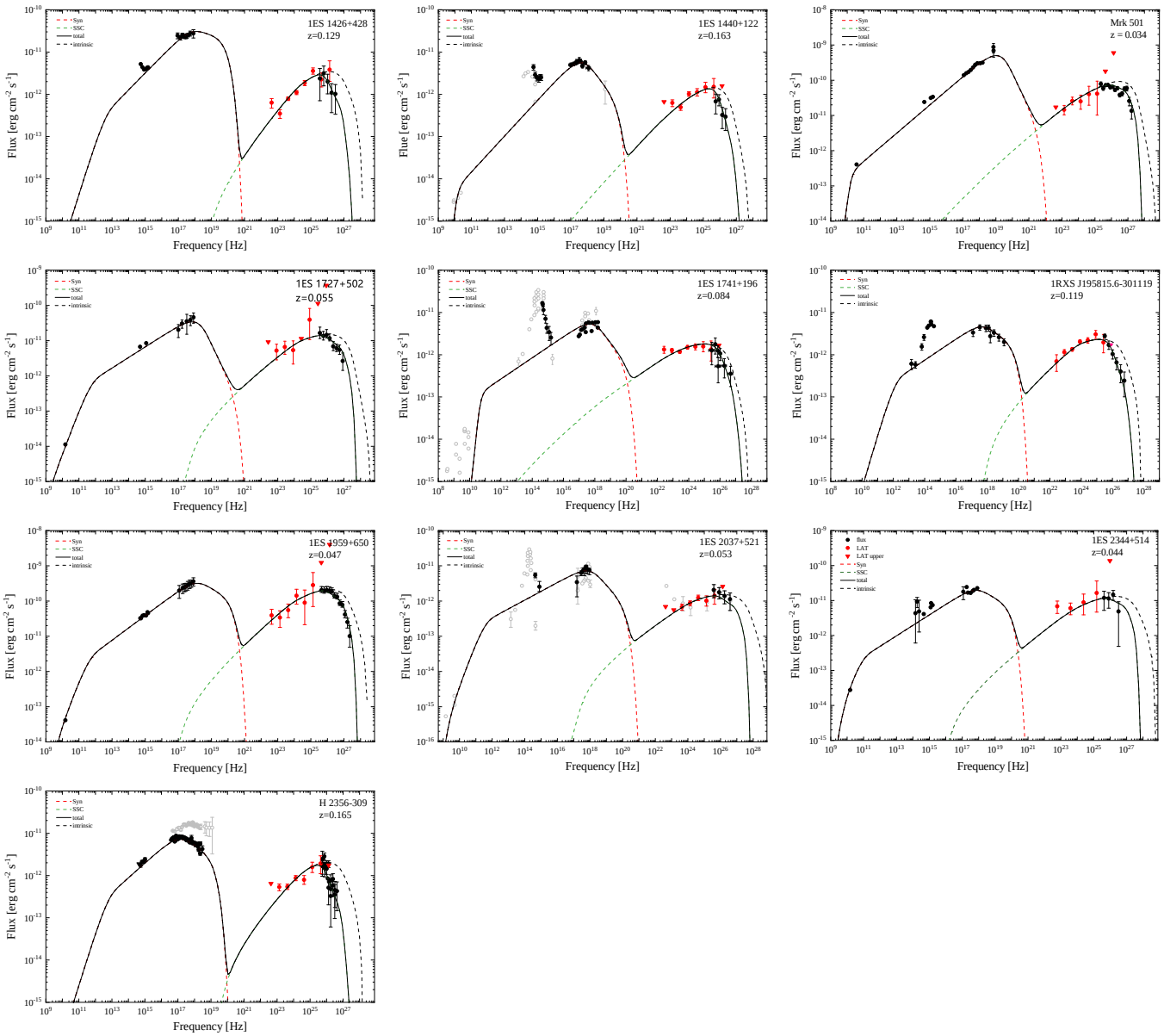

Figure 2. (Continued.)

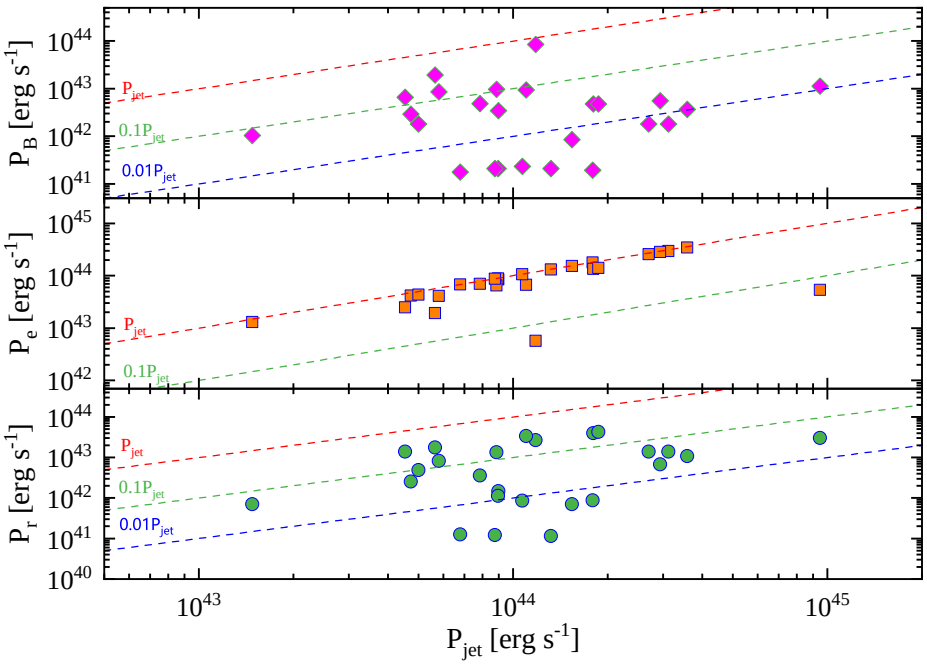

Figure 3. P_r, P_e, and P_B as functions of P_{jet} for the 25 EHBLs.

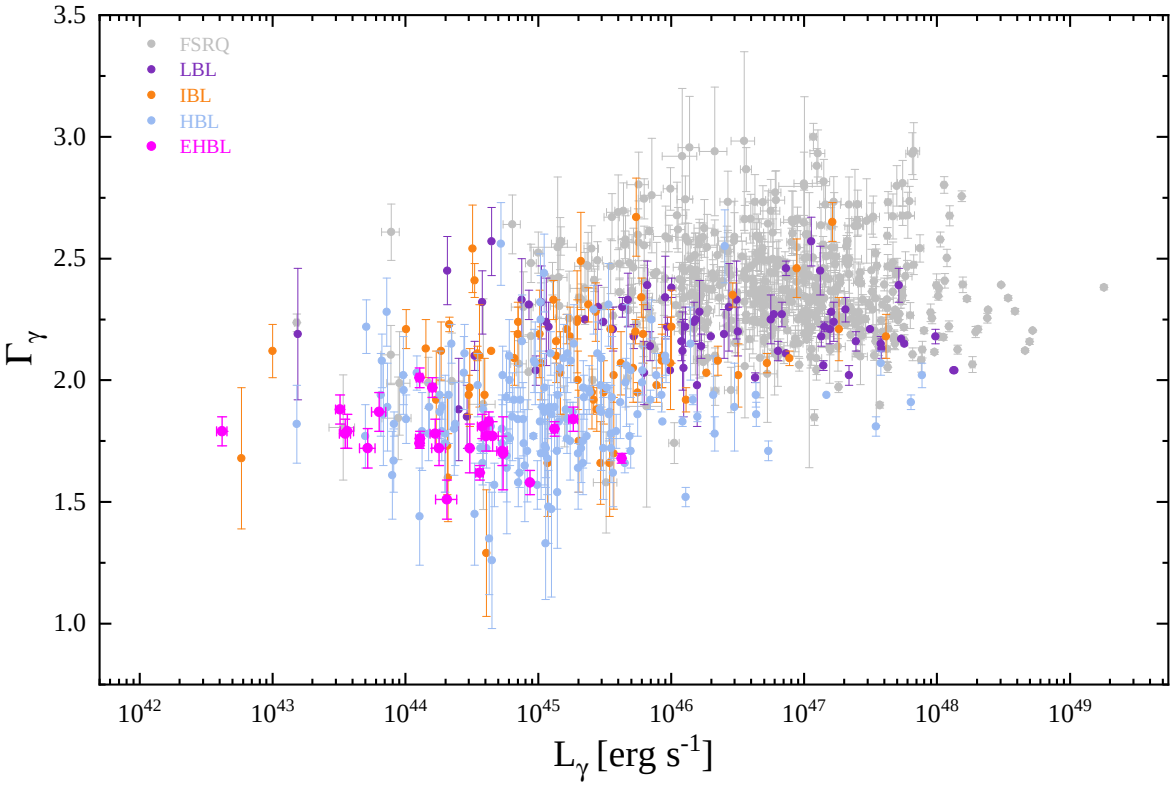

Figure 4. The photon spectral index (Γ_γ) versus the γ-ray average luminosity (L_γ). Data for FSRQs, LBLs, IBLs, HBLs are taken from the 4FGL-DR3 (Abdollahi et al. 2022).

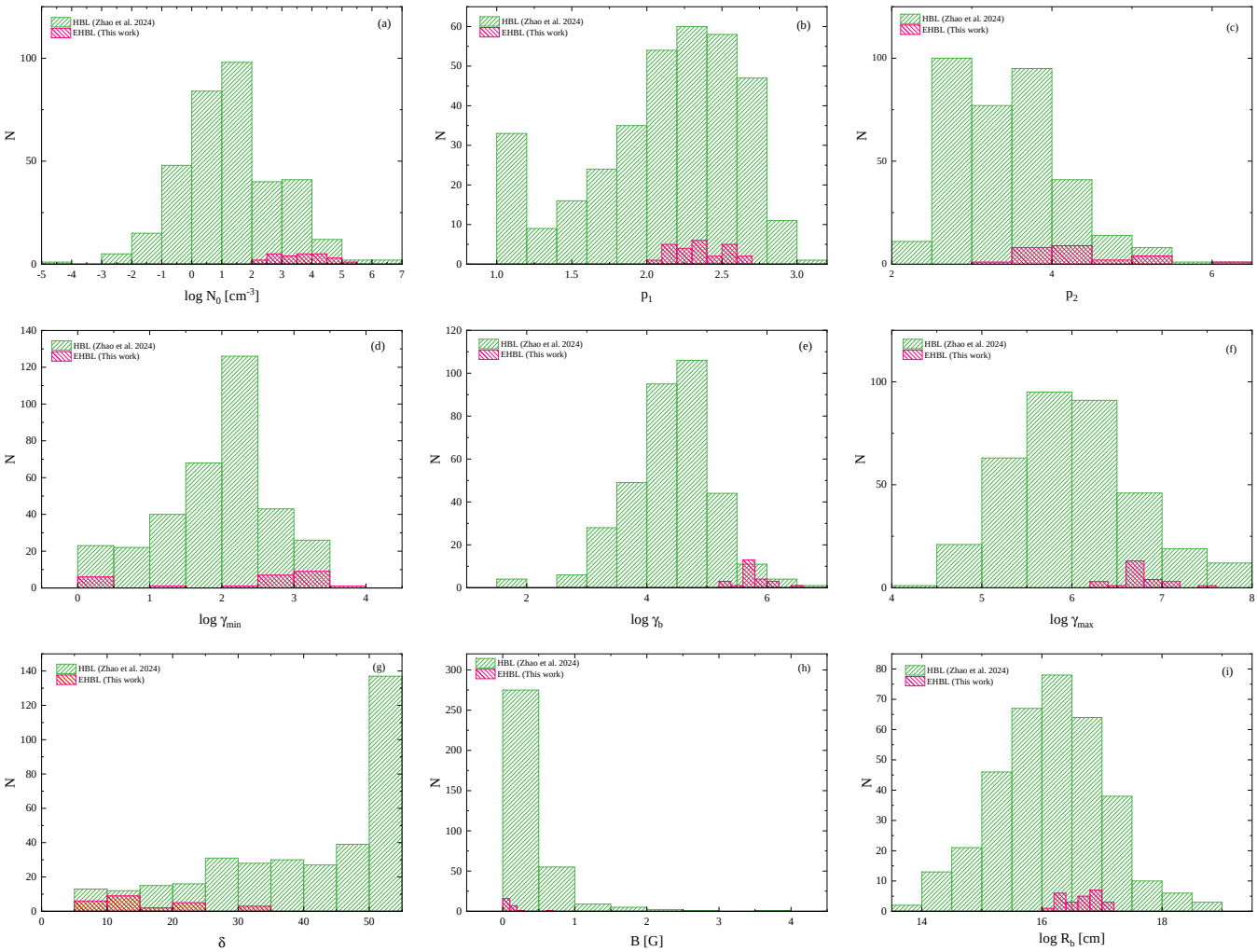

Figure 5. The distributions of the SED fitting parameters for the 25 EHBLs are represented by red shaded regions. For comparison, the corresponding parameter data for a HBL sample from Zhao et al. (2024) are also shown, indicated by green shaded regions.

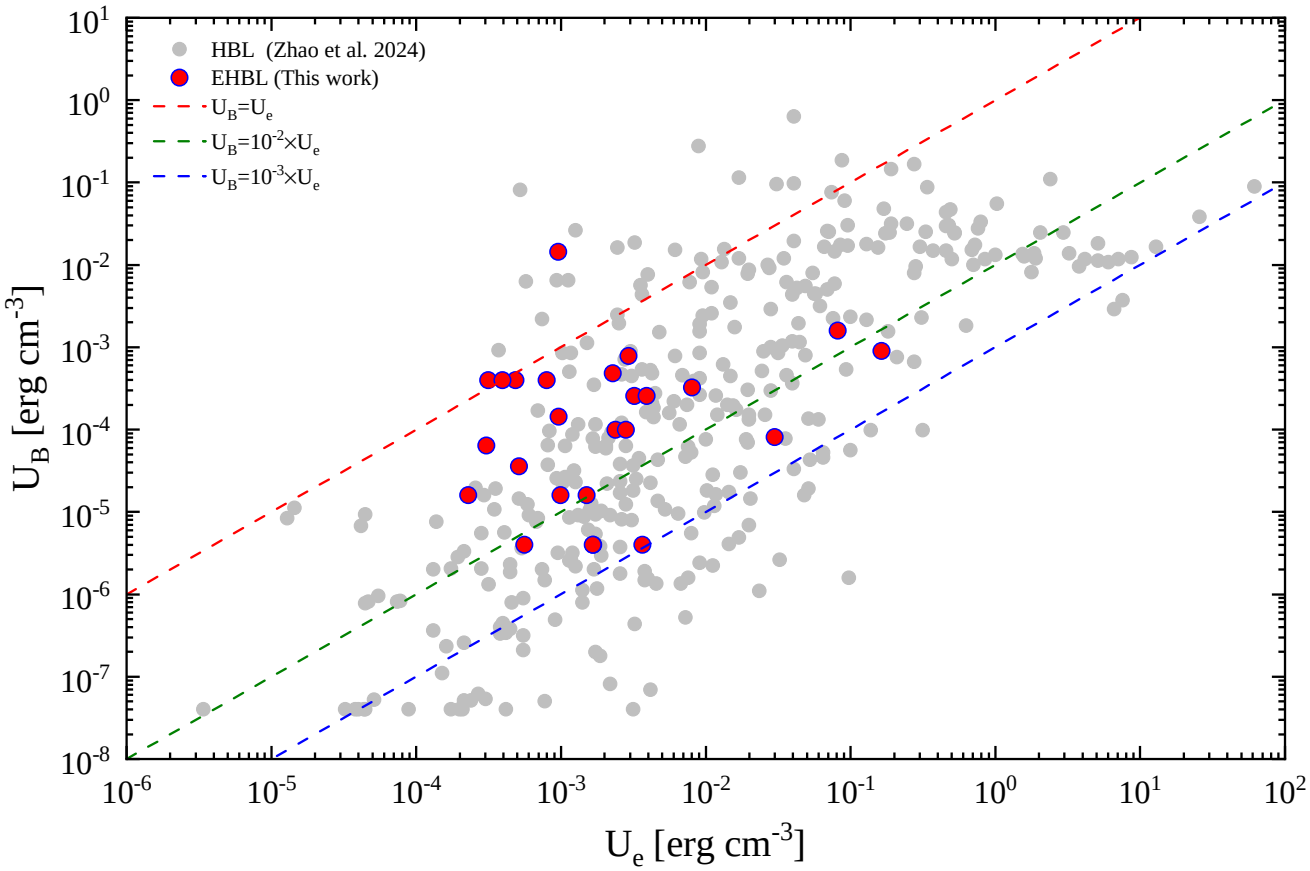

Figure 6. U_B as a function of U_e for the 25 EHBLs (red circles). For comparison, the corresponding parameter data for a HBL sample from Zhao et al. (2024) are also included (gray circles).

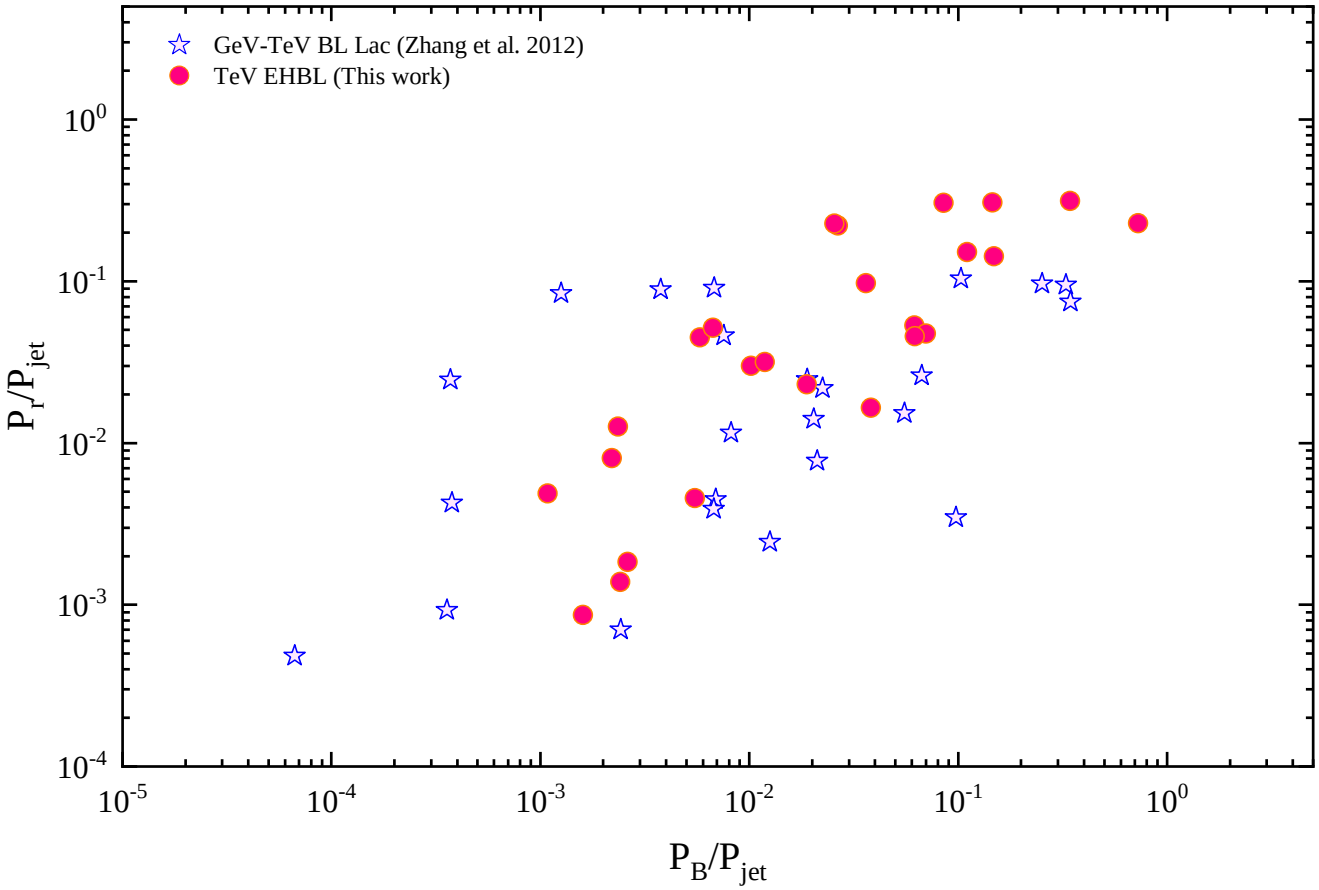

Figure 7. P_r/P_{jet} as a function of P_B/P_{jet} for the 25 EHBLs (red circles). For comparison, the data for a GeV-TeV BL Lac sample from Zhang et al. (2012) are also included (blue stars).

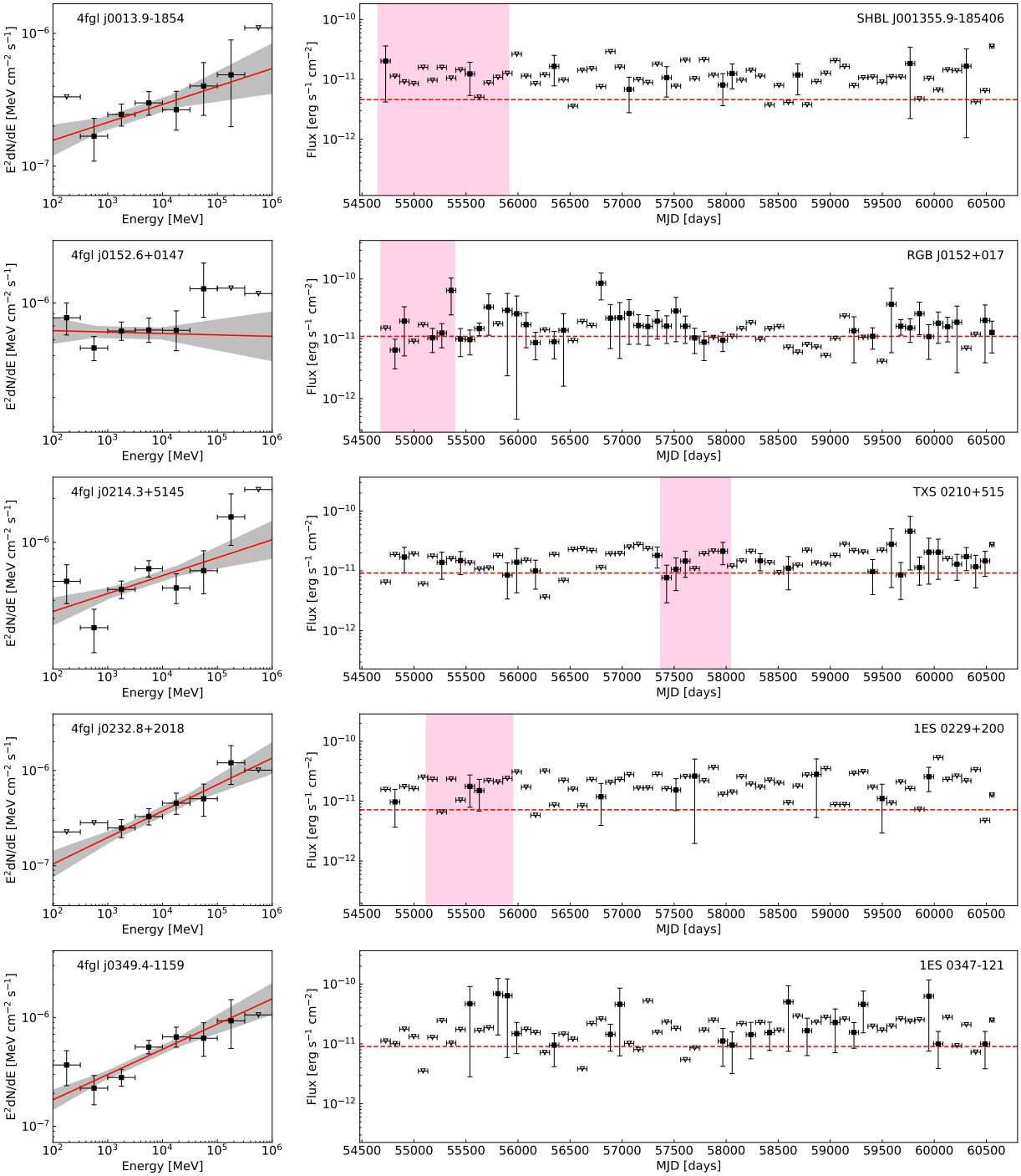
4fgl j0013.9-1854
SHBL J001355.9-185406
4fgl j0152.6+0147
RGB J0152+017
4fgl j0214.3+5145
TXS 0210+515
4fgl j0232.8+2018
1ES 0229+200
4fgl j0349.4-1159
1ES 0347-121
E²dN/dE [MeV cm⁻² s⁻¹]
Energy [MeV]
Flux [erg s⁻¹ cm⁻²]
MJD [days]

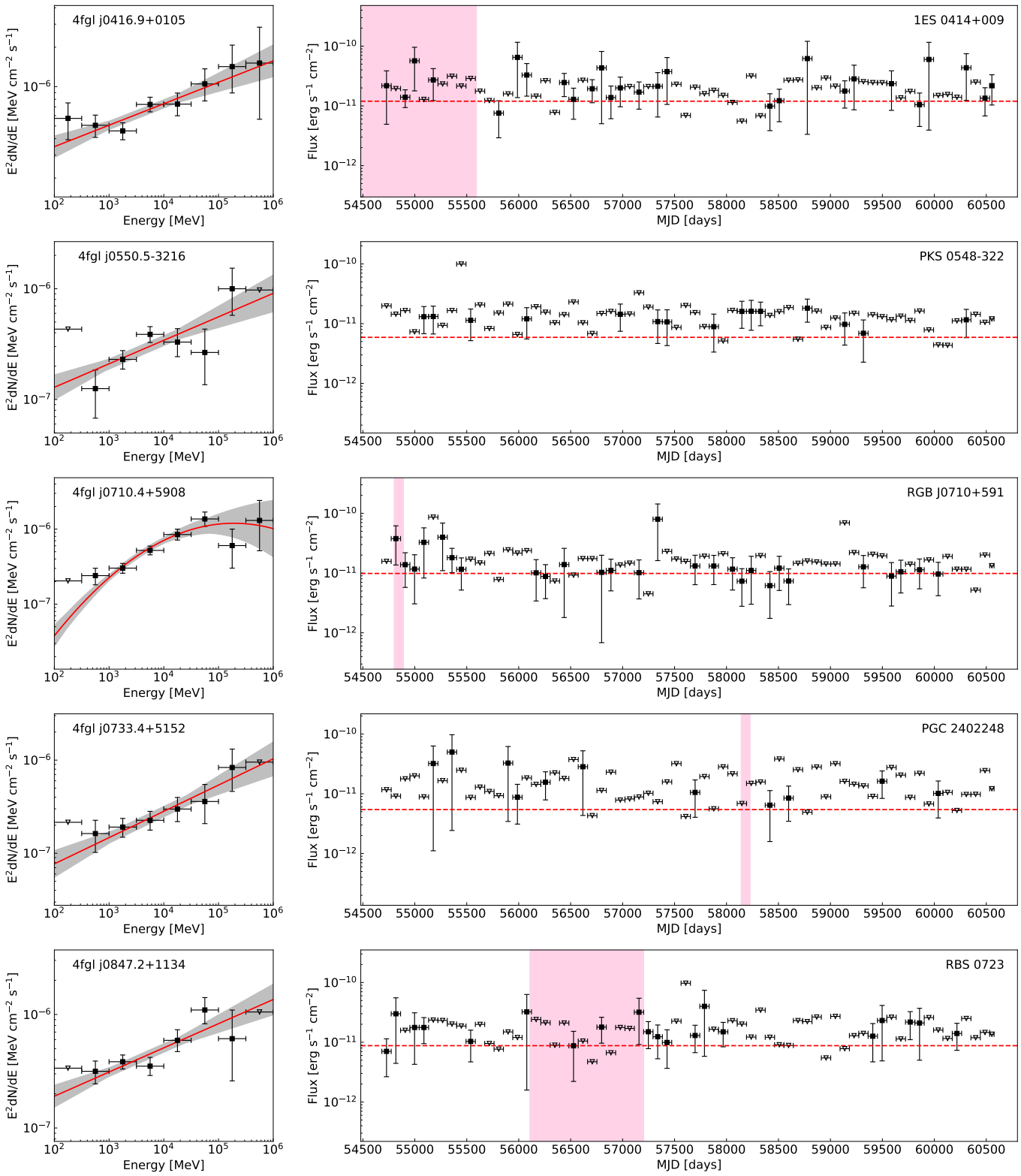
4fgl j0416.9+0105
1ES 0414+009
4fgl j0550.5-3216
PKS 0548-322
4fgl j0710.4+5908
RGB J0710+591
4fgl j0733.4+5152
PGC 2402248
4fgl j0847.2+1134
RBS 0723
E²dN/dE [MeV cm⁻² s⁻¹]
Energy [MeV]
Flux [erg s⁻¹ cm⁻²]
MJD [days]

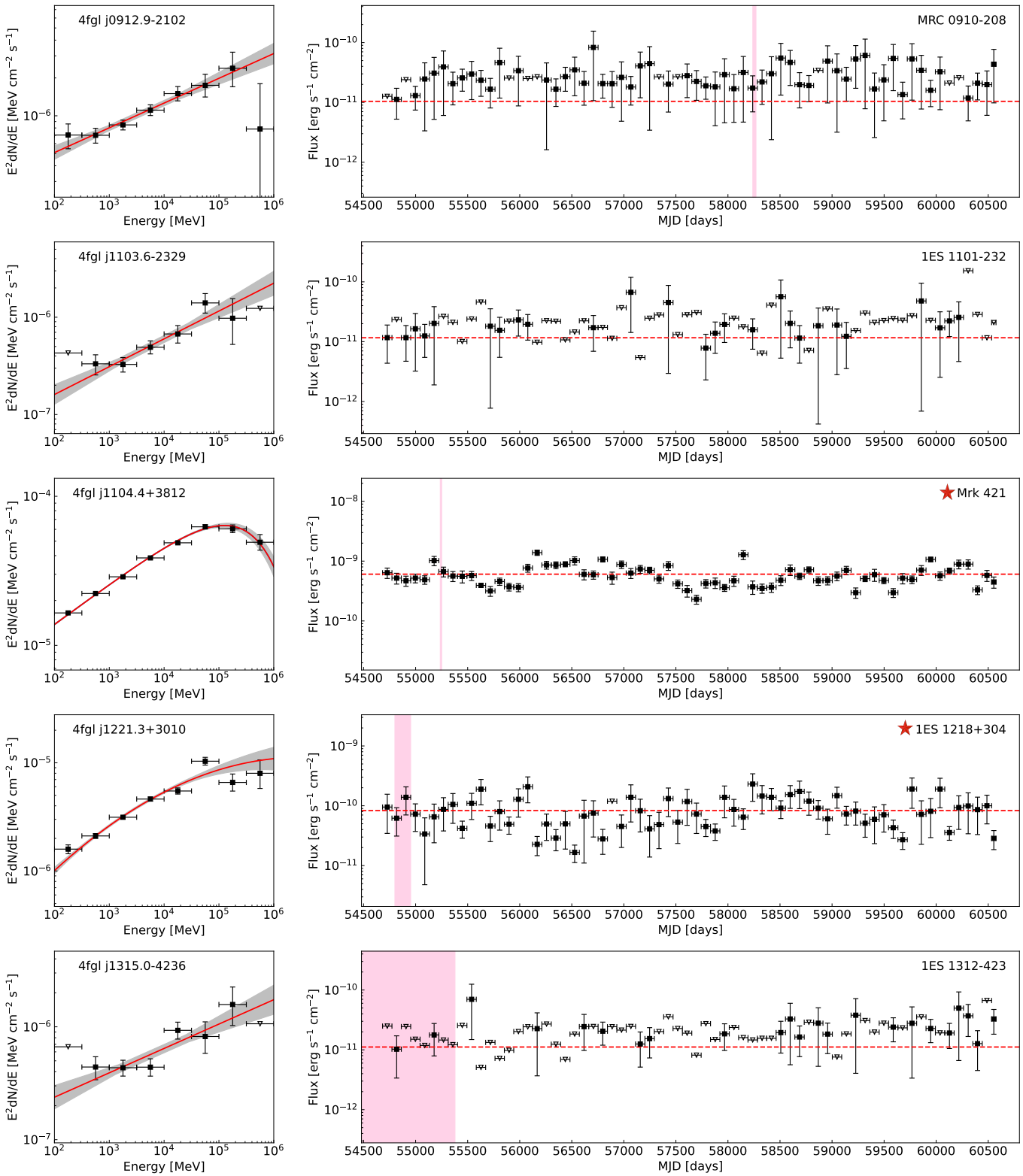
4fgl j0912.9-2102
MRC 0910-208
4fgl j1103.6-2329
1ES 1101-232
4fgl j1104.4+3812
Mrk 421
4fgl j1221.3+3010
1ES 1218+304
4fgl j1315.0-4236
1ES 1312-423
E²dN/dE [MeV cm⁻² s⁻¹]
Energy [MeV]
Flux [erg s⁻¹ cm⁻²]
MJD [days]

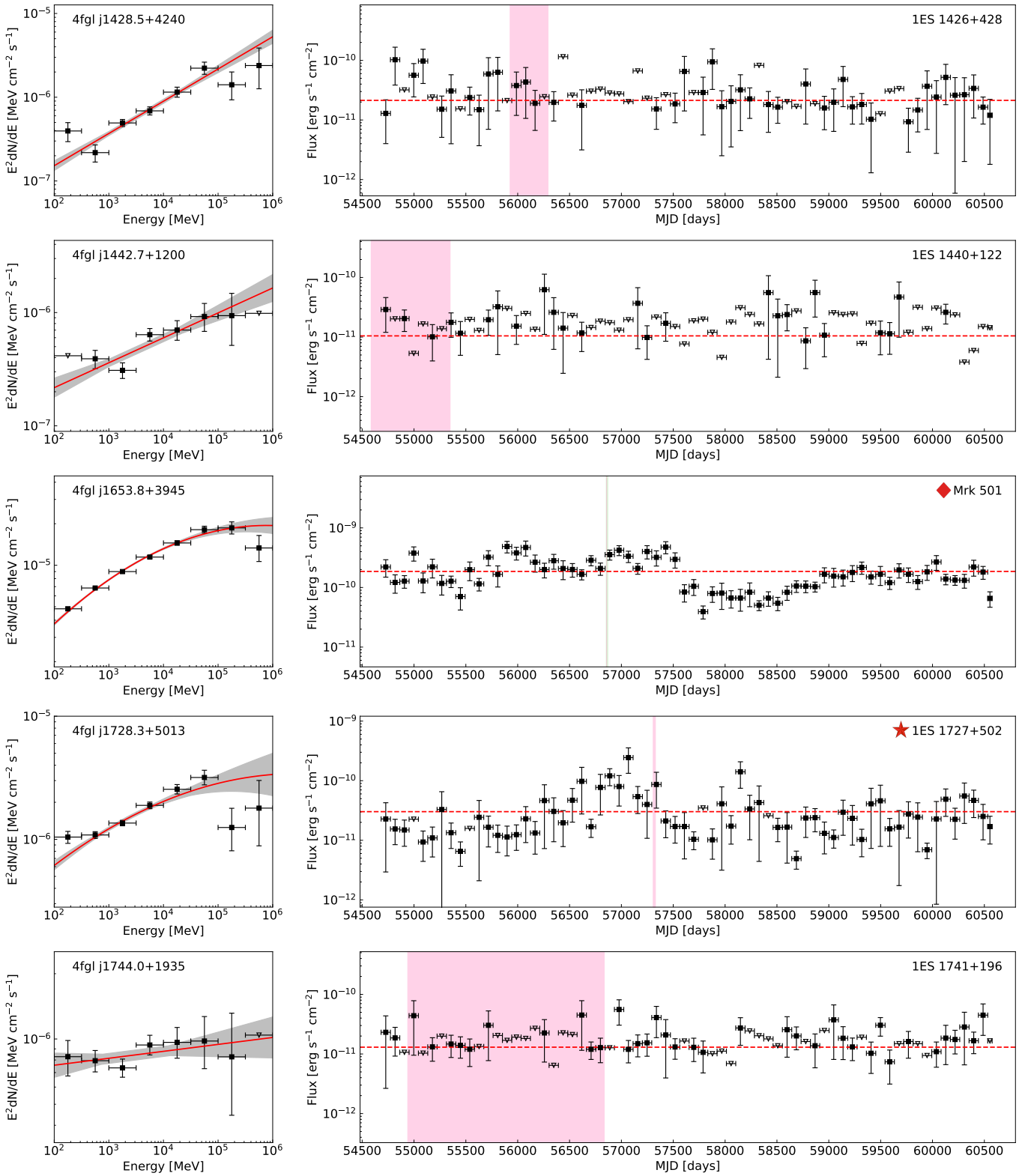
4fgl j1428.5+4240
1ES 1426+428
4fgl j1442.7+1200
1ES 1440+122
4fgl j1653.8+3945
Mrk 501
4fgl j1728.3+5013
1ES 1727+502
4fgl j1744.0+1935
1ES 1741+196
E²dN/dE [MeV cm⁻² s⁻¹]
Energy [MeV]
Flux [erg s⁻¹ cm⁻²]
MJD [days]

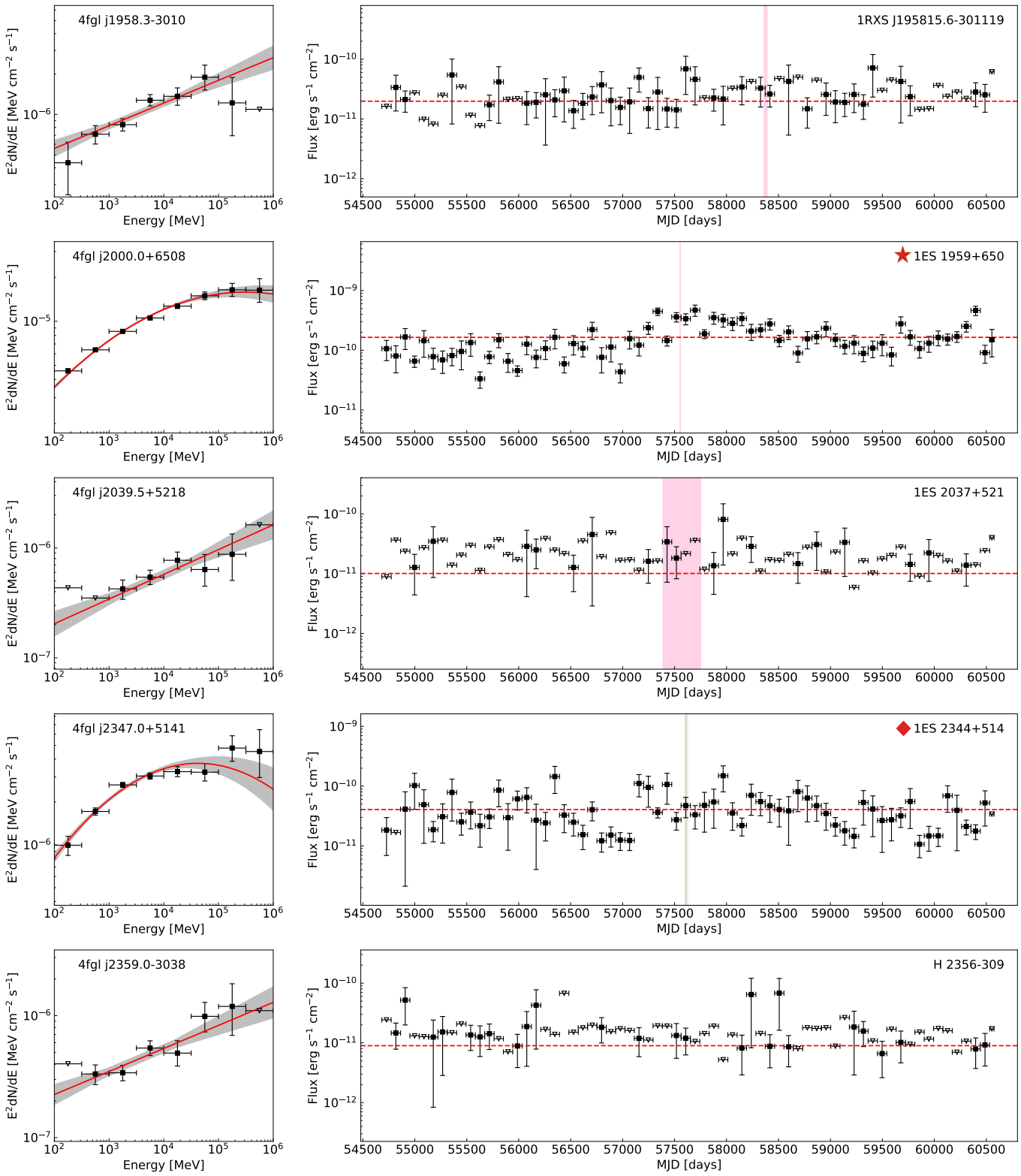
4fgl j1958.3-3010
1RXS J195815.6-301119
4fgl j2000.0+6508
1ES 1959+650
4fgl j2039.5+5218
1ES 2037+521
4fgl j2347.0+5141
1ES 2344+514
4fgl j2359.0-3038
H 2356-309
E²dN/dE [MeV cm⁻² s⁻¹]
Energy [MeV]
Flux [erg s⁻¹ cm⁻²]
MJD [days]

REFERENCES

Abdo, A. A., Ackermann, M., Agudo, I., et al. 2010, ApJ, 716, 30, doi: 10.1088/0004-637X/716/1/30

Abdo, A. A., Ackermann, M., Ajello, M., et al. 2011, ApJ, 727, 129, doi: 10.1088/0004-637X/727/2/129

Abdollahi, S., Acero, F., Ackermann, M., et al. 2020, ApJS, 247, 33, doi: 10.3847/1538-4365/ab6bcb

Abdollahi, S., Acero, F., Baldini, L., et al. 2022, ApJS, 260, 53, doi: 10.3847/1538-4365/ac6751

Abeysekara, A. U., Archambault, S., Archer, A., et al. 2016, MNRAS, 459, 2550, doi: 10.1093/mnras/stw664

—. 2017, ApJ, 834, 2, doi: 10.3847/1538-4357/834/1/2

Acciari, V. A., Aliu, E., Arlen, T., et al. 2009, ApJ, 695, 1370, doi: 10.1088/0004-637X/695/2/1370

—. 2010a, ApJL, 715, L49, doi: 10.1088/2041-8205/715/1/L49

Acciari, V. A., Aliu, E., Beilicke, M., et al. 2010b, ApJL, 709, L163, doi: 10.1088/2041-8205/709/2/L163

Acciari, V. A., Aliu, E., Arlen, T., et al. 2011, ApJ, 738, 169, doi: 10.1088/0004-637X/738/2/169

Acciari, V. A., Ansoldi, S., Antonelli, L. A., et al. 2020, ApJS, 247, 16, doi: 10.3847/1538-4365/ab5b98

Acero, F., Ackermann, M., Ajello, M., et al. 2015, ApJS, 218, 23, doi: 10.1088/0067-0049/218/2/23

Ackermann, M., Ajello, M., Allafort, A., et al. 2011, ApJ, 743, 171, doi: 10.1088/0004-637X/743/2/171

—. 2013, ApJS, 209, 34, doi: 10.1088/0067-0049/209/2/34

Ackermann, M., Ajello, M., Atwood, W. B., et al. 2015, ApJ, 810, 14, doi: 10.1088/0004-637X/810/1/14

Aguilar-Ruiz, E., Fraija, N., Galván-Gámez, A., & Benítez, E. 2022, MNRAS, 512, 1557, doi: 10.1093/mnras/stac591

Aharonian, F., Akhperjanian, A. G., Bazer-Bachi, A. R., et al. 2006, A&A, 455, 461, doi: 10.1051/0004-6361:20054732

Aharonian, F., Akhperjanian, A. G., Barres de Almeida, U., et al. 2007a, A&A, 473, L25, doi: 10.1051/0004-6361:20078412

Aharonian, F., Akhperjanian, A. G., Bazer-Bachi, A. R., et al. 2007b, A&A, 470, 475, doi: 10.1051/0004-6361:20077057

Aharonian, F., Akhperjanian, A. G., Barres de Almeida, U., et al. 2007c, A&A, 475, L9, doi: 10.1051/0004-6361:20078462

—. 2008, A&A, 481, L103, doi: 10.1051/0004-6361:200809603

Aharonian, F., Akhperjanian, A. G., Anton, G., et al. 2010, A&A, 521, A69, doi: 10.1051/0004-6361/200912363

Aharonian, F. A. 2004, Very high energy cosmic gamma radiation : a crucial window on the extreme Universe, doi: 10.1142/4657

Ahn, C. P., Alexandroff, R., Allende Prieto, C., et al. 2012, ApJS, 203, 21, doi: 10.1088/0067-0049/203/2/21

Ahnen, M. L., Ansoldi, S., Antonelli, L. A., et al. 2017, MNRAS, 468, 1534, doi: 10.1093/mnras/stx472

—. 2018, A&A, 620, A181, doi: 10.1051/0004-6361/201833704

Albert, A., Alfaro, R., Alvarez, C., et al. 2022, ApJ, 929, 125, doi: 10.3847/1538-4357/ac58f6

Albert, J., Aliu, E., Anderhub, H., et al. 2006, ApJL, 642, L119, doi: 10.1086/504845

—. 2007a, ApJ, 669, 862, doi: 10.1086/521382

—. 2007b, ApJ, 662, 892, doi: 10.1086/518431

Aleksić, J., Antonelli, L. A., Antoranz, P., et al. 2014, A&A, 563, A90, doi: 10.1051/0004-6361/201321360

Aleksić, J., Ansoldi, S., Antonelli, L. A., et al. 2015, A&A, 573, A50, doi: 10.1051/0004-6361/201322906

Aliu, E., Archambault, S., Arlen, T., et al. 2012, ApJ, 755, 118, doi: 10.1088/0004-637X/755/2/118

—. 2014a, ApJ, 782, 13, doi: 10.1088/0004-637X/782/1/13

—. 2014b, ApJ, 797, 89, doi: 10.1088/0004-637X/797/2/89

Allen, C., Archambault, S., Archer, A., et al. 2017, MNRAS, 471, 2117, doi: 10.1093/mnras/stx1756

Amenomori, M., Ayabe, S., Cui, S. W., et al. 2003, ApJ, 598, 242, doi: 10.1086/378350

Archambault, S., Archer, A., Beilicke, M., et al. 2015, ApJ, 808, 110, doi: 10.1088/0004-637X/808/2/110

Archambault, S., Archer, A., Barnacka, A., et al. 2016, MNRAS, 461, 202, doi: 10.1093/mnras/stw1319

Bade, N., Beckmann, V., Douglas, N. G., et al. 1998, A&A, 334, 459, doi: 10.48550/arXiv.astro-ph/9803204

Banerjee, B., Joshi, M., Majumdar, P., et al. 2019, MNRAS, 487, 845, doi: 10.1093/mnras/stz1292

Baumgartner, W. H., Tueller, J., Markwardt, C. B., et al. 2013, ApJS, 207, 19, doi: 10.1088/0067-0049/207/2/19

Biteau, J., Prandini, E., Costamante, L., et al. 2020, Nature Astronomy, 4, 124, doi: 10.1038/s41550-019-0988-4

Blandford, R., & Eichler, D. 1987, PhR, 154, 1, doi: 10.1016/0370-1573(87)90134-7

Błażejowski, M., Sikora, M., Moderski, R., & Madejski, G. M. 2000, ApJ, 545, 107, doi: 10.1086/317791

Bloom, S. D., & Marscher, A. P. 1996, ApJ, 461, 657, doi: 10.1086/177092

Blumenthal, G. R., & Gould, R. J. 1970, Reviews of Modern Physics, 42, 237, doi: 10.1103/RevModPhys.42.237

Bonnoli, G., Tavecchio, F., Ghisellini, G., & Sbarrato, T. 2015, MNRAS, 451, 611, doi: 10.1093/mnras/stv953

Bony (de), M., Bylund, T., Meyer, M., et al. 2022, in 37th International Cosmic Ray Conference, 823, doi: 10.22323/1.395.0823

Catanese, M., Akerlof, C. W., Badran, H. M., et al. 1998, ApJ, 501, 616, doi: 10.1086/305857

Cerruti, M., Zech, A., Boisson, C., & Inoue, S. 2015, MNRAS, 448, 910, doi: 10.1093/mnras/stu2691

Chen, L. 2017, ApJ, 842, 129, doi: 10.3847/1538-4357/aa7744

Chen, P. S., Fu, H. W., & Gao, Y. F. 2005, NewA, 11, 27, doi: 10.1016/j.newast.2005.05.004

Condon, J. J., Cotton, W. D., Greisen, E. W., et al. 1998, AJ, 115, 1693, doi: 10.1086/300337

Costamante, L., Bonnoli, G., Tavecchio, F., et al. 2018, MNRAS, 477, 4257, doi: 10.1093/mnras/sty857

Costamante, L., & Ghisellini, G. 2002, A&A, 384, 56, doi: 10.1051/0004-6361:20011749

Costamante, L., Ghisellini, G., Giommi, P., et al. 2001a, A&A, 371, 512, doi: 10.1051/0004-6361:20010412

Costamante, L., Ghisellini, G., Giommi, P., et al. 2001b, in American Institute of Physics Conference Series, Vol. 599, X-ray Astronomy: Stellar Endpoints, AGN, and the Diffuse X-ray Background, ed. N. E. White, G. Malaguti, & G. G. C. Palumbo, 586–589, doi: 10.1063/1.1434692

Das, S., Gupta, N., & Razzaque, S. 2020, ApJ, 889, 149, doi: 10.3847/1538-4357/ab6131

de Vaucouleurs, G., de Vaucouleurs, A., Corwin, Herold G., J., et al. 1991, Third Reference Catalogue of Bright Galaxies

Dermer, C. D., & Menon, G. 2009, High Energy Radiation from Black Holes: Gamma Rays, Cosmic Rays, and Neutrinos

Dermer, C. D., Schlickeiser, R., & Mastichiadis, A. 1992, A&A, 256, L27

Dmytriiev, A., Sol, H., & Zech, A. 2021, MNRAS, 505, 2712, doi: 10.1093/mnras/stab1445

Donato, D., Sambruna, R. M., & Gliozzi, M. 2005, A&A, 433, 1163, doi: 10.1051/0004-6361:20034555

Falomo, R. 1991, AJ, 101, 821, doi: 10.1086/115726

Falomo, R., & Kotilainen, J. K. 1999, A&A, 352, 85, doi: 10.48550/arXiv.astro-ph/9910106

Falomo, R., Pesce, J. E., & Treves, A. 1995, ApJL, 438, L9, doi: 10.1086/187702

Falomo, R., Scarpa, R., & Bersanelli, M. 1994, ApJS, 93, 125, doi: 10.1086/192048

Falomo, R., Scarpa, R., Treves, A., & Urry, C. M. 2000, ApJ, 542, 731, doi: 10.1086/317044

Fan, J. H. 2003, ApJL, 585, L23, doi: 10.1086/374033

Fan, J. H., Yang, J. H., Liu, Y., et al. 2016, ApJS, 226, 20, doi: 10.3847/0067-0049/226/2/20

Finke, J. D., Ajello, M., Domínguez, A., et al. 2022, ApJ, 941, 33, doi: 10.3847/1538-4357/ac9843

Foffano, L., Prandini, E., Franceschini, A., & Paiano, S. 2019, MNRAS, 486, 1741, doi: 10.1093/mnras/stz812

Forman, W., Jones, C., Cominsky, L., et al. 1978, ApJS, 38, 357, doi: 10.1086/190561

Fortson, L., VERITAS Collaboration, & Fermi-LAT Collaborators. 2012, in American Institute of Physics Conference Series, Vol. 1505, High Energy Gamma-Ray Astronomy: 5th International Meeting on High Energy Gamma-Ray Astronomy, ed. F. A. Aharonian, W. Hofmann, & F. M. Rieger (AIP), 514–517, doi: 10.1063/1.4772310

Fossati, G., Buckley, J. H., Bond, I. H., et al. 2008, ApJ, 677, 906, doi: 10.1086/527311

Ghisellini, G. 2013, Radiative Processes in High Energy Astrophysics, Vol. 873, doi: 10.1007/978-3-319-00612-3

Ghisellini, G., Celotti, A., & Costamante, L. 2002, A&A, 386, 833, doi: 10.1051/0004-6361:20020275

Ghisellini, G., Celotti, A., Fossati, G., Maraschi, L., & Comastri, A. 1998, MNRAS, 301, 451, doi: 10.1046/j.1365-8711.1998.02032.x

Ghisellini, G., & Tavecchio, F. 2009, MNRAS, 397, 985, doi: 10.1111/j.1365-2966.2009.15007.x

Ghisellini, G., Tavecchio, F., Foschini, L., et al. 2010, MNRAS, 402, 497, doi: 10.1111/j.1365-2966.2009.15898.x

Giacconi, R., Murray, S., Gursky, H., et al. 1972, ApJ, 178, 281, doi: 10.1086/151790

Gioia, I. M., Henry, J. P., Maccacaro, T., et al. 1990, ApJL, 356, L35, doi: 10.1086/185744

Giommi, P., Ansari, S. G., & Micol, A. 1995, A&AS, 109, 267

Giommi, P., Padovani, P., & Perlman, E. 2000, MNRAS, 317, 743, doi: 10.1046/j.1365-8711.2000.03353.x

Giommi, P., Padovani, P., Polenta, G., et al. 2012, MNRAS, 420, 2899, doi: 10.1111/j.1365-2966.2011.20044.x

Giommi, P., Tagliaferri, G., Beuermann, K., et al. 1991, ApJ, 378, 77, doi: 10.1086/170408

Goswami, P., Zacharias, M., Zech, A., et al. 2024, A&A, 682, A134, doi: 10.1051/0004-6361/202348121

Gursky, H., Bradt, H., Doxsey, R., et al. 1978, ApJ, 223, 973, doi: 10.1086/156329

H. E. S. S. Collaboration, Abramowski, A., Acero, F., et al. 2010, A&A, 516, A56, doi: 10.1051/0004-6361/201014321

—. 2012, A&A, 538, A103, doi: 10.1051/0004-6361/201118406

—. 2013, A&A, 554, A72, doi: 10.1051/0004-6361/201220996

Halpern, J. P., Chen, V. S., Madejski, G. M., & Chanan, G. A. 1991, AJ, 101, 818, doi: 10.1086/115725

Hartman, R. C., Bertsch, D. L., Bloom, S. D., et al. 1999, ApJS, 123, 79, doi: 10.1086/313231

HESS Collaboration, Abramowski, A., Acero, F., et al. 2013, MNRAS, 434, 1889, doi: 10.1093/mnras/stt1081

Holder, J., Bond, I. H., Boyle, P. J., et al. 2003, ApJL, 583, L9, doi: 10.1086/367816

Jones, D. H., Read, M. A., Saunders, W., et al. 2009, MNRAS, 399, 683, doi: 10.1111/j.1365-2966.2009.15338.x

Jones, F. C. 1968, Physical Review, 167, 1159, doi: 10.1103/PhysRev.167.1159

Kapanadze, B., Romano, P., Vercellone, S., et al. 2016, MNRAS, 457, 704, doi: 10.1093/mnras/stv3004

Kapanadze, B., Dorner, D., Vercellone, S., et al. 2018, MNRAS, 473, 2542, doi: 10.1093/mnras/stx2492

Katarzyński, K., Ghisellini, G., Tavecchio, F., Gracia, J., & Maraschi, L. 2006, MNRAS, 368, L52, doi: 10.1111/j.1745-3933.2006.00156.x

Katarzyński, K., Sol, H., & Kus, A. 2001, A&A, 367, 809, doi: 10.1051/0004-6361:20000538

Kaur, N., Chandra, S., Baliyan, K. S., Sameer, & Ganesh, S. 2017, ApJ, 846, 158, doi: 10.3847/1538-4357/aa86b0

Láinez, M., Nievas-Rosillo, M., Domínguez, A., et al. 2025, A&A, 700, A229, doi: 10.1051/0004-6361/202554155

Laurent-Muehleisen, S. A., Kollgaard, R. I., Feigelson, E. D., Brinkmann, W., & Siebert, J. 1999, ApJ, 525, 127, doi: 10.1086/307881

Lewis, T. R., Finke, J. D., & Becker, P. A. 2018, ApJ, 853, 6, doi: 10.3847/1538-4357/aaa19a

Li, X.-P., Luo, Y.-H., Yang, H.-Y., et al. 2017, ApJ, 847, 8, doi: 10.3847/1538-4357/aa86ee

Liu, J.-R., Wang, J.-M., Fermi-LAT Collaboration, et al. 2025, Nature Astronomy, 9, 1086, doi: 10.1038/s41550-025-02538-2

MAGIC Collaboration, Acciari, V. A., Ansoldi, S., et al. 2019, MNRAS, 490, 2284, doi: 10.1093/mnras/stz2725

—. 2020a, A&A, 637, A86, doi: 10.1051/0004-6361/201834603

—. 2020b, MNRAS, 496, 3912, doi: 10.1093/mnras/staa1702

—. 2020c, A&A, 640, A132, doi: 10.1051/0004-6361/202037811

—. 2021, A&A, 655, A89, doi: 10.1051/0004-6361/202141004

MAGIC Collaboration, Abe, H., Abe, S., et al. 2024, A&A, 682, A114, doi: 10.1051/0004-6361/202347845

Mankuzhiyil, N., Persic, M., & Franceschini, A. 2023, MNRAS, 524, 133, doi: 10.1093/mnras/stad1858

Mao, L. S. 2011, NewA, 16, 503, doi: 10.1016/j.newast.2011.05.002

Maraschi, L., Ghisellini, G., & Celotti, A. 1992, ApJL, 397, L5, doi: 10.1086/186531

Marscher, A. P., Jorstad, S. G., D'Arcangelo, F. D., et al. 2008, Nature, 452, 966, doi: 10.1038/nature06895

Massaro, F., Paggi, A., Errando, M., et al. 2013, ApJS, 207, 16, doi: 10.1088/0067-0049/207/1/16

Mastichiadis, A., & Kirk, J. G. 1997, A&A, 320, 19, doi: 10.48550/arXiv.astro-ph/9610058

Mastichiadis, A., Petropoulou, M., & Dimitrakoudis, S. 2013, MNRAS, 434, 2684, doi: 10.1093/mnras/stt1210

Medina-Carrillo, B., Sahu, S., Sánchez-Colón, G., & Rajpoot, S. 2023, MNRAS, 519, 854, doi: 10.1093/mnras/stac3591

NASA/IPAC Extragalactic Database (NED). 2019, NASA/IPAC Extragalactic Database (NED), IPAC, doi: 10.26132/NED1

Neronov, A., Semikoz, D., & Taylor, A. M. 2012, A&A, 541, A31, doi: 10.1051/0004-6361/201117083

Nievas Rosillo, M., Domínguez, A., Chiaro, G., et al. 2022, MNRAS, 512, 137, doi: 10.1093/mnras/stac491

Nilsson, K., Pursimo, T., Heidt, J., et al. 2003, A&A, 400, 95, doi: 10.1051/0004-6361:20021861

Nishiyama, T. 1999, in International Cosmic Ray Conference, Vol. 3, 26th International Cosmic Ray Conference (ICRC26), Volume 3, ed. D. Kieda, M. Salamon, & B. Dingus, 370

Nolan, P. L., Abdo, A. A., Ackermann, M., et al. 2012, ApJS, 199, 31, doi: 10.1088/0067-0049/199/2/31

Padovani, P., Alexander, D. M., Assef, R. J., et al. 2017, A&A Rv, 25, 2, doi: 10.1007/s00159-017-0102-9

Patel, S. R., Shukla, A., Chitnis, V. R., et al. 2018, A&A, 611, A44, doi: 10.1051/0004-6361/201731987

Peng, F.-K., Zhang, H.-M., Wang, X.-Y., Wang, J.-F., & Zhi, Q.-J. 2019, ApJ, 884, 91, doi: 10.3847/1538-4357/ab3e6f

Perlman, E. S., Stocke, J. T., Schachter, J. F., et al. 1996, ApJS, 104, 251, doi: 10.1086/192300

Perri, M., Maselli, A., Giommi, P., et al. 2007, A&A, 462, 889, doi: 10.1051/0004-6361:20066063

Prandini, E., & MAGIC Collaboration. 2019, Mem. Soc. Astron. Italiana, 90, 164, doi: 10.48550/arXiv.1908.02154

Punch, M., Akerlof, C. W., Cawley, M. F., et al. 1992, Nature, 358, 477, doi: 10.1038/358477a0

Quinn, J., Akerlof, C. W., Biller, S., et al. 1996, ApJL, 456, L83, doi: 10.1086/309878

Rector, T. A., Stocke, J. T., Perlman, E. S., Morris, S. L., & Gioia, I. M. 2000, AJ, 120, 1626, doi: 10.1086/301587

Remillard, R. A., Tuohy, I. R., Brissenden, R. J. V., et al. 1989, ApJ, 345, 140, doi: 10.1086/167888

Rüger, M., Spanier, F., & Mannheim, K. 2010, MNRAS, 401, 973, doi: 10.1111/j.1365-2966.2009.15738.x

Rybicki, G. B., & Lightman, A. P. 1979, Radiative processes in astrophysics

Sbarufatti, B., Falomo, R., Treves, A., & Kotilainen, J. 2006, A&A, 457, 35, doi: 10.1051/0004-6361:20065455

Scarpa, R., Urry, C. M., Falomo, R., Pesce, J. E., & Treves, A. 2000, ApJ, 532, 740, doi: 10.1086/308618

Schachter, J. F., Stocke, J. T., Perlman, E., et al. 1993, ApJ, 412, 541, doi: 10.1086/172942

Schwope, A., Hasinger, G., Lehmann, I., et al. 2000, Astronomische Nachrichten, 321, 1, doi: 10.1002/(SICI)1521-3994(200003)321:1<1::AID-ASNA1>3.0.CO;2-C

Shukla, A., Chitnis, V. R., Vishwanath, P. R., et al. 2012, A&A, 541, A140, doi: 10.1051/0004-6361/201118569

Shukla, A., Chitnis, V. R., Singh, B. B., et al. 2015, ApJ, 798, 2, doi: 10.1088/0004-637X/798/1/2

Sikora, M., Begelman, M. C., & Rees, M. J. 1994, ApJ, 421, 153, doi: 10.1086/173633

Sikora, M., Stawarz, Ł., Moderski, R., Nalewajko, K., & Madejski, G. M. 2009, ApJ, 704, 38, doi: 10.1088/0004-637X/704/1/38

Singh, K., Meintjes, P., Ramamonjisoa, F., & Tolamatti, A. 2019, NewA, 73, 101278, doi: 10.1016/j.newast.2019.101278

Sol, H., & Zech, A. 2022, Galaxies, 10, 105, doi: 10.3390/galaxies10060105

Stickel, M., Padovani, P., Urry, C. M., Fried, J. W., & Kuehr, H. 1991, ApJ, 374, 431, doi: 10.1086/170133

Stocke, J. T., Morris, S. L., Gioia, I. M., et al. 1991, ApJS, 76, 813, doi: 10.1086/191582

Tanaka, Y. T., Stawarz, Ł., Finke, J., et al. 2014, ApJ, 787, 155, doi: 10.1088/0004-637X/787/2/155

Tavecchio, F., Costa, A., & Sciaccaluga, A. 2022, MNRAS, 517, L16, doi: 10.1093/mnrasl/slac084

Tavecchio, F., Ghisellini, G., Ghirlanda, G., Foschini, L., & Maraschi, L. 2010, MNRAS, 401, 1570, doi: 10.1111/j.1365-2966.2009.15784.x

Tramacere, A., Giommi, P., Massaro, E., et al. 2007, A&A, 467, 501, doi: 10.1051/0004-6361:20066226

Urry, C. M., & Padovani, P. 1995, PASP, 107, 803, doi: 10.1086/133630

Voges, W., Aschenbach, B., Boller, T., et al. 1996, IAUC, 6420, 2

Wang, G., Xiao, H., Fan, J., & Zhang, X. 2024a, ApJS, 270, 22, doi: 10.3847/1538-4365/ad0e08

Wang, Z.-R., Xue, R., Xiong, D., et al. 2024b, ApJS, 271, 10, doi: 10.3847/1538-4365/ad168c

Wood, K. S., Meekins, J. F., Yentis, D. J., et al. 1984, ApJS, 56, 507, doi: 10.1086/190992

Wood, M., Caputo, R., Charles, E., et al. 2017, in International Cosmic Ray Conference, Vol. 301, 35th International Cosmic Ray Conference (ICRC2017), 824, doi: 10.22323/1.301.0824

Xue, R., Wang, Z.-R., & Li, W.-J. 2022, PhRvD, 106, 103021, doi: 10.1103/PhysRevD.106.103021

Yan, D., Zeng, H., & Zhang, L. 2014, MNRAS, 439, 2933, doi: 10.1093/mnras/stu146

Yuan, Y. H., Fan, J. H., & Pan, H. J. 2015, AJ, 150, 67, doi: 10.1088/0004-6256/150/3/67

Yuan, Y.-h., & Liu, F.-q. 2014, ChA&A, 38, 233, doi: 10.1016/j.chinastron.2014.07.001

Zhang, J. 2009, Research in Astronomy and Astrophysics, 9, 777, doi: 10.1088/1674-4527/9/7/006

Zhang, J., Liang, E.-W., Zhang, S.-N., & Bai, J. M. 2012, ApJ, 752, 157, doi: 10.1088/0004-637X/752/2/157

Zhang, J., Sun, X.-N., Liang, E.-W., et al. 2014, ApJ, 788, 104, doi: 10.1088/0004-637X/788/2/104

Zhang, Y.-H., & Li, J.-C. 2017, MNRAS, 469, 1682, doi: 10.1093/mnras/stx942

Zhao, X. Z., Yang, H. Y., Zheng, Y. G., & Kang, S. J. 2024, ApJ, 967, 104, doi: 10.3847/1538-4357/ad3ba9

Żywucka, N., Goyal, A., Jamrozy, M., Ostrowski, M., & Stawarz, Ł. 2014, A&A, 563, A135, doi: 10.1051/0004-6361/201423500

APPENDIX

A. DETAILS OF THE SAMPLE

- *SHBL J001355.9–185406.* The extreme blazar SHBL J001355.9–185406 is located at a redshift of z = 0.095 (Jones et al. 2009), with equatorial coordinates (J2000) of R.A. = 3.483641° and Dec. = -18.901918°. The equatorial coordinates of the sources in this appendix are all taken from the NASA/IPAC Extragalactic Database (NED) (2019)[4]. SHBL J001355.9—185406 was first detected in X-rays by ROSAT with flux in the 0.1–2.4 keV band is 1.26×10^{-11} erg s^{-1} cm^{-2} (1RXS J001356.6–185408, Voges et al. 1996) and later identified as a BL Lac object by Schwope et al. (2000). The TeV γ-ray flux was measured at approximately 1% of the Crab nebula flux above 300 GeV (H. E. S. S. Collaboration et al. 2013). Fermi-LAT did not detect a high-energy counterpart in 0.1-300 GeV for the initial two years of operation (Nolan et al. 2012). At 1.4 GHz, the radio flux density is 29.2 ± 1.0 mJy (Condon et al. 1998). The low-frequency radio spectrum is even flatter, with a spectral index -0.1 ± 0.1 down to 156 MHz, suggesting that the jet exhibits a self-similar structure up to relatively large distances from the jet base (Żywucka et al. 2014).

- *RGB J0152+017.* The extreme blazar RGB J0152+017 is located at a redshift of z = 0.080 (Laurent-Muehleisen et al. 1999), with equatorial coordinates (J2000) of R.A. = 28.165046° and Dec. = 1.788162° in an elliptical galaxy with luminosity $M_R = -24.0$ (Nilsson et al. 2003). Its TeV γ-ray emission was discovered by the Cherenkov telescope array H.E.S.S. in November 2007, showing no significant variation and a flux of 2.6×10^{-12} cm^{-2} s^{-1} above 300 GeV; the X-ray and UV flux varies on time scales of ~ 10 days (Aharonian et al. 2008).

- *TXS 0210+515.* The extreme blazar TXS 0210+515 is located at a redshift of z = 0.049 (Mao 2011), with equatorial coordinates (J2000) of R.A. = 33.574725° and Dec. = 51.747763°. According to the MAGIC observations, the intrinsic spectral index of TXS 0210+515 is 1.6 ± 0.3 and it is classified as a hard-TeV EHBL (Acciari et al. 2020).

- *1ES 0229+200.* The extreme blazar 1ES 0229+200 resides in a faint elliptical host galaxy with luminosity $M_R = -24.53$ (Falomo et al. 2000) at a redshift of z = 0.139 (Massaro et al. 2013). The position of 1ES 0229+200 in Equatorial (J2000) coordinates is R.A. = 38.202562° and Dec. = 20.288193°. It was initially classified as HBL in 1995 after its discovery in 1992 by the Einstein Slew Survey (Giommi et al. 1995). The TeV γ-ray emission from 1ES 0229+200 was first discovered by the H.E.S.S. observations during the period of 2005–2006 (Aharonian et al. 2007c). As a prototypical EHBL, the spectrum of 1ES 0229+200 was measured to extend up to 10 TeV with a hard archival spectral index at TeV of 2.5 ± 0.19 (Aharonian et al. 2007c).

- *1ES 0347–121.* The extreme blazar 1ES 0347–121 was classified as a BL Lac object in 1993 after its discovery in 1992 by the Einstein Slew Survey (Schachter et al. 1993). It resides in an elliptical host galaxy with luminosity $M_R = -23.2$ (Falomo & Kotilainen 1999) at redshift z = 0.188 (Massaro et al. 2013). The position of 1ES 0347–121 in Equatorial (J2000) coordinates is R.A.=57.346623° and Dec.=-11.990914°. The first TeV γ-ray emission was discovered by H.E.S.S. telescopes in 2006 above an energy threshold of 250 GeV (Aharonian et al. 2007a).

- *1ES 0414+009.* The extreme blazar 1ES 0414+009 resides in an elliptical galaxy (Halpern et al. 1991) at a redshift of z = 0.287 (Halpern et al. 1991), with equatorial coordinates (J2000) of R.A. = 64.218722° and Dec. = 1.089972°. It is one of the most distant TeV BL Lacs detected to date. 1ES 0414+009 was first detected by the HEAO-1 satellite (Gursky et al. 1978) in the energy range of 0.2 keV–10 MeV and was detected for the first time in the TeV band in 2005 by H.E.S.S. observations. The TeV γ-ray emission is observed both by the H.E.S.S. (Aliu et al. 2012) and VERITAS (H. E. S. S. Collaboration et al. 2012) collaborations.

- *PKS 0548–322.* The extreme blazar PKS 0548–322 resides in a giant elliptical galaxy with an absolute visual magnitude of $M_V = -23.4$ (Falomo et al. 1995) at a redshift of z = 0.069 (Massaro et al. 2013), with equatorial coordinates (J2000) of R.A. = 87.669037° and Dec. = -32.271197°. PKS 0548–322 was not detected in the MeV-GeV range by the EGRET detector (Hartman et al. 1999), but it is suggested as a candidate TeV emitter by Costamante & Ghisellini (2002). The first discovery of TeV γ-rays from PKS 0548–322 was made using the H.E.S.S. Cherenkov telescopes, as presented in Aharonian et al. (2010). The details about the X-ray history of this object can be found in Perri et al. (2007).

[4] https://ned.ipac.caltech.edu/.

- *RGB J0710+591.* The extreme blazar RGB J0710+591 was first discovered by HEAO A-1 (Wood et al. 1984), hosted in an elliptical galaxy with a nuclear point source at redshift z = 0.125 (Giommi et al. 1991; Scarpa et al. 2000). The position of RGB J0710+591 in Equatorial (J2000) is R.A. = 107.629000°, Dec. = 59.139000°. Its first TeV emission was detected by VERITAS during the 2008-2009 observations with no evidence of variability in the γ-ray light curve above 300 GeV (Acciari et al. 2010a).

- *PGC 2402248.* The extreme blazar PGC 2402248 is located at a redshift of z = 0.065 (Mankuzhiyil et al. 2023), with equatorial coordinates (J2000) of R.A. = 113.361630°, Dec. = 51.898871°. The MAGIC telescopes observed the source from January 23 to April 19, 2018 (MJD 58141–58227). During this period, simultaneous broadband observations were also carried out by the KVA and the Swift/UVOT in the optical and ultraviolet bands, Swift/XRT in the X-ray band, and Fermi-LAT in the GeV γ-ray band, which showed no significant variability except for moderate variability in the Swift-UVOT/XRT data (Medina-Carrillo et al. 2023).

- *RBS 0723.* The extreme blazar RBS 0723 is a BL Lac object at z = 0.198 (Ahn et al. 2012), identified as a bright X-ray source in the ROSAT All Sky Survey and characterized by a hard ($\alpha = 0.78$) X-ray continuum as observed by Swift/XRT (Ackermann et al. 2013). Its equatorial coordinates (J2000) are R.A. = 131.803899° and Dec. = 11.563962°. RBS 0723 is included in the 1FHL and 2FHL catalogs, exhibiting a hard spectral index $\Gamma_{\rm 1FHL} = 1.4 \pm 0.4$ and a bright gamma-ray flux (9.6×10^{-11} ph cm^{-2} s^{-1}) above 10 GeV (Ackermann et al. 2013). The MAGIC telescopes detected TeV γ-rays from RBS 0723 during observations conducted in 2013 and 2014, with a flux of $2.6 \pm 0.5 \times 10^{-12}$ ph cm^{-2} s^{-1} above 200 GeV (Acciari et al. 2020).

- *MRC 0910–208.* The extreme blazar MRC 0910-208 is located at a redshift of z = 0.198 (Massaro et al. 2013), with equatorial coordinates (J2000) of R.A. = 138.250930° and Dec. = -21.055861°. Its TeV γ-rays were observed by H.E.S.S. in May 2018, with a spectral index of 3.63 (Bony (de) et al. 2022).

- *1ES 1101–232.* The extreme blazar 1ES 1101–232 was first detected by the Ariel-5 X-ray satellite, hosted in an elliptical host galaxy at a redshift of z = 0.186 (Falomo et al. 1994). The position of 1ES 1101–232 in Equatorial (J2000) is R.A. = 165.906738°, Dec. = -23.491975°. The discovery of TeV γ-ray emission from this source was reported in 2007 using H.E.S.S. observations performed during 2004-2005 in the energy range above 250 GeV, and no significant variation of the TeV γ-ray flux on any time scale was found (Aharonian et al. 2007b).

- *Mrk 421.* The nearest extreme blazar Mrk 421 located at the redshift of z = 0.031 (MAGIC Collaboration et al. 2021) is one of the most extensively studied and brightest extragalactic γ-ray sources. The position of Mrk 421 in Equatorial (J2000) is R.A.=166.113808°, Dec.=38.208833°. It is also one of the fastest varying γ-ray sources. The observations about Mrk 421 are provided by various instruments that covering the energy range from radio to TeV γ-ray (e.g., Amenomori et al. 2003; Fossati et al. 2008; Mastichiadis et al. 2013; Abeysekara et al. 2017. Its TeV γ-rays was firstly detected by the Whipple telescope in 1992 above 0.5 TeV (Punch et al. 1992).

- *1ES 1218+304.* The extreme blazar 1ES 1218+304 is located at a redshift of z = 0.182 (Bade et al. 1998), with equatorial coordinates (J2000) of R.A. = 185.341432° and Dec. = 30.176983°. The TeV γ-rays were first observed by MAGIC (Albert et al. 2006) and subsequently by the VERITAS telescopes (Acciari et al. 2009). The γ-ray emission at $\sim$ 160 GeV and $\sim$ 1.8 TeV is characterized by a hard γ-ray photon index of 1.86 ± 0.37 after EBL correction (Acciari et al. 2009). The first evidence of variability in the TeV γ-ray emission from 1ES 1218+304 was observed by VERITAS during the active state in 2009, with a flux doubling time-scale of $\leqslant$ 1 day (Acciari et al. 2010b). 1ES 1218+304 exhibits a hard photon index of 1.72 ± 0.02 as observed by Fermi-LAT in the GeV γ-ray band (Abdollahi et al. 2020).

- *1ES 1312–423.* The extreme blazar 1ES 1312–423, located at a redshift of z = 0.105 (Rector et al. 2000), was initially detected in X-rays by the Einstein observatory (Gioia et al. 1990) and subsequently classified as a BL Lac object by Stocke et al. (1991). The position of 1ES 1312–423 in equatorial coordinates (J2000) is R.A. = 198.764134°, Dec. = -42.613821°. Between April 2004 and July 2010, it was observed by H.E.S.S. in the TeV γ-ray band above 280 GeV, with a spectral index of $\Gamma = 2.85 \pm 0.47$ and a differential flux at 1 TeV of $F = 1.89 \pm 0.58 \times 10^{-13}$ cm^{-2} s^{-1} TeV^{-1} (HESS Collaboration et al. 2013).

- *1ES 1426+428.* The extreme blazar 1ES 1426+428 is located at a redshift of z = 0.129 (Wang et al. 2024a), with equatorial coordinates (J2000) of R.A. = 217.135851° and Dec. = 42.672493°. It was first detected in X-rays by the Uhuru X-ray

observatory (Giacconi et al. 1972) and was classified as a BL Lac by Remillard et al. (1989) based on the combined observations of featureless optical continua, compact radio emission, and images of the underlying host galaxies. 1ES 1426+428 has a synchrotron peak at $10^{18.1}$ Hz (Costamante et al. 2001b) and is characterized by being optically faint but very bright in the X-ray band.

- *1ES 1440+122.* The extreme blazar 1ES 1440+122, located at a redshift of z = 0.163 (Sbarufatti et al. 2006), is identified as an extreme-high-synchrotron-peaked BL Lac object with a synchrotron peak frequency of $\nu_{s,p} \sim 3 \times 10^{17}$ Hz (Archambault et al. 2016). The position of 1ES 1440+122 in equatorial coordinates (J2000) is R.A. = 220.700901°, Dec. = 12.011167°. 1ES 1440+122 was included in the 3FGL catalogue (3FGL J1442.8+1200) with a spectral index of 1.80 ± 0.12(Acero et al. 2015).

- *Mrk 501.* The extreme blazar Mrk 501, located at a redshift of z = 0.034 (Wang et al. 2024a), is also a very well-studied TeV source, similar to Mrk 421. It has been intensively monitored by various astronomical detectors, from radio frequencies to TeV γ-rays (e.g., Abdo et al. 2011; Neronov et al. 2012; Aleksić et al. 2015; Shukla et al. 2015; Ahnen et al. 2018; Albert et al. 2022). The position of Mrk 501 in equatorial coordinates (J2000) is R.A. = 253.467569°, Dec. = 39.760169°. Its TeV γ-rays were first detected by the Whipple telescope in 1996 at energies above 0.3 TeV (Quinn et al. 1996).

- *1ES 1727+502.* The extreme blazar 1ES 1727+502 is a nearby BL Lac located at a redshift of z = 0.055 (de Vaucouleurs et al. 1991). The position of 1ES 1727+502 in equatorial coordinates (J2000) is R.A. = 262.077600°, Dec. = 50.219575°. Its TeV γ-rays were discovered by MAGIC, with an integral flux above 150 GeV estimated to be (2.1 ± 0.4)% of the Crab nebula flux. The de-absorbed TeV spectrum has a photon index of (2.7 ± 0.5) (Aleksić et al. 2014). It was also detected by VERITAS, with an integral flux of $(1.1 \pm 0.2) \times 10^{-11}$ cm^{-2} s^{-1} above 250 GeV (Archambault et al. 2015). 1ES 1727+502 shows little variability in the optical R-band, is bright in the X-ray band, and has a hard spectrum in the GeV γ-ray band (Aleksić et al. 2014).

- *1ES 1741+196.* The extreme blazar 1ES 1741+196 is a nearby BL Lac located at a redshift of z = 0.084 (Perlman et al. 1996). The position of 1ES 1741+196 in equatorial coordinates (J2000) is R.A. = 265.990971°, Dec. = 19.585839°. TeV γ-ray emission was first detected by the MAGIC collaboration (Ahnen et al. 2017). It was included in the 3LAC catalogue as HBL 3FGL J1743.9+1934, with a spectral index of $\Gamma = 1.777 \pm 0.108$ (Ackermann et al. 2015).

- *1RXS J195815.6–301119.* The extreme blazar 1RXS J195815.6–301119 is located at a redshift of z = 0.119 (Bony (de) et al. 2022), with equatorial coordinates (J2000) of R.A. = 299.562136° and Dec. = -30.186556°. Its TeV γ-rays were observed by H.E.S.S. in May 2018, with a spectral index of 2.78 (Bony (de) et al. 2022).

- *1ES 1959+650.* The extreme blazar 1ES 1959+650, located at a redshift of z = 0.047 (Wang et al. 2024a), is one of the earliest extragalactic TeV γ-ray emitters (Holder et al. 2003), whose TeV emission was first detected in 1998 (Nishiyama 1999). The position of 1ES 1959+650 in equatorial coordinates (J2000) is R.A. = 299.999383°, Dec. = 65.148514°. Observations revealed that 1ES 1959+650 is very active across multiple wavebands (Aliu et al. 2014b; Yuan & Liu 2014; Yuan et al. 2015; Kapanadze et al. 2016, 2018; Kaur et al. 2017; Li et al. 2017; Zhang & Li 2017; Patel et al. 2018).

- *1ES 2037+521.* The extreme blazar 1ES 2037+521 is located at a redshift of z = 0.053 (Wang et al. 2024a), with equatorial coordinates (J2000) of R.A. = 309.847998° and Dec. = 52.330608°. It was observed with the MAGIC telescopes in 2016, showing a flux of $(1.8 \pm 0.4) \times 10^{-12}$ erg cm^{-2} s^{-1} and an EBL-corrected spectral index of 2.0 ± 0.5. It was also observed with Swift-XRT, showing a flux in the 2–10 keV band of $(10.7 \pm 1.0) \times 10^{-12}$ erg cm^{-2} s^{-1} and a spectral index of 1.93 ± 0.13. It was observed with Fermi-LAT, showing a flux in the 1–300 GeV energy range of $(4.6 \pm 1.5) \times 10^{-10}$ erg cm^{-2} s^{-1} and a spectral index of 1.7 ± 0.2 (Acciari et al. 2020).

- *1ES 2344+514.* The extreme blazar 1ES 2344+514 is a nearby BL Lac located at a redshift of z = 0.044 (Perlman et al. 1996), with equatorial coordinates (J2000) of R.A. = 356.770154° and Dec. = 51.704967°. The first TeV detection was achieved by the Whipple 10 m telescope during a bright flare in 1996, with a peak flux of approximately 60% of the Crab Nebula flux above 350 GeV (Catanese et al. 1998). Then, Allen et al. (2017) reported an average flux above 350 GeV of approximately 4% of the Crab Nebula between 2008 and 2015, during a period without any flaring activity. MAGIC Collaboration et al. (2024) reported that MAGIC observations from August 2019 to December 2021 revealed strong spectral variability occurring in the quiescent state. They also reported a strong X-ray flare, among the brightest observed from MAGIC. The TeV flux can vary by a factor of approximately 2 on daily timescales (Albert et al. 2007b;

Allen et al. 2017; Acciari et al. 2011), and it is highly variable in X-rays over timescales as short as 5000 seconds (Giommi et al. 2000).

- *H 2356–309.* The extreme blazar H 2356–309 is one of the most distant BL Lacs, hosted by a normal giant elliptical galaxy located at a redshift of z = 0.165 (Falomo 1991), with equatorial coordinates (J2000) of R.A. = 359.782919° and Dec. = -30.627960°. It was first observed in X-rays by the UHURU satellite (Forman et al. 1978). The TeV γ-rays were discovered by H.E.S.S. during June to December 2004 (Aharonian et al. 2006).

B. MODEL DESCRIPTION

The model assumes a spherical, uniformly emitting region with a radius of R and a magnetic field of B, which moves along the jet with the bulk Lorentz factor Γ. The angle between the jet and the observer's line of sight is $1/\Gamma$, and the Doppler beaming factor δ is considered to be equal to Γ.

B.1. *Electron Energy Distribution*

The steady electron energy distribution (EED) within this region is modeled as a broken power law without restricting the specific acceleration process.

$$N(\gamma) = N_0 \begin{cases} \gamma^{-p_1} & \gamma_{\rm min} \leqslant \gamma \leqslant \gamma_{\rm b}, \\ \gamma_{\rm b}^{p_2-p_1}\gamma^{-p_2} & \gamma_{\rm b} < \gamma < \gamma_{\rm max}, \end{cases} \tag{B1}$$

where p_1 and p_2 are the electron spectral indices, $\gamma_{\rm min}$, γ_b, and $\gamma_{\rm max}$ are the electron Lorentz factors, and N_0 [cm^{-3}] denotes the electron number density.

B.2. *Synchrotron*

Single particle synchrotron emissivity [erg s^{-1} Hz^{-1}] (Ghisellini 2013) is

$$P_{\rm syn}(\nu,\gamma) = \frac{2\pi\sqrt{3}e^2\nu_{\rm L}}{c}\left[\frac{\nu}{\nu_{\rm c}}\int_{\nu/\nu_{\rm c}}^{\infty} K_{5/3}(t)dt\right], \tag{B2}$$

where Larmor frequency $\nu_{\rm L} = \frac{eB}{2\pi m_e c}$, critical frequency $\nu_{\rm c} = \frac{3}{2}\nu_{\rm s}$, synchrotron radiation frequency $\nu_{\rm s} = \gamma^2\nu_{\rm L}$. $K_{5/3}(t)$ is the modified Bessel function of order 5/3. The synchrotron emissivity coefficient from many electrons averaged over an isotropic distribution of pitch angles is given by [erg s^{-1} cm^{-3} Hz^{-1} ster^{-1}] (Rybicki & Lightman 1979)

$$j_{\rm syn}(\nu) = \frac{1}{4\pi}\int P_{\rm syn}(\nu,\gamma)N(\gamma){\rm d}\gamma. \tag{B3}$$

Synchrotron self-absorption (SSA) coefficient $\kappa(\nu)$[cm^{-1}] (Rybicki & Lightman 1979) is obtained by

$$\kappa(\nu) = -\frac{1}{8\pi m_{\rm e}\nu^2}\int_{\gamma_{\rm min}}^{\gamma_{\rm max}} P_{\rm syn}(\nu,\gamma)\gamma^2\frac{d}{d\gamma}\left[\frac{N(\gamma)}{\gamma^2}\right]d\gamma. \tag{B4}$$

The optical depth caused by SSA is $\tau = \kappa(\nu)R$, and when $\tau < 10^{-4}$, the SSA is ignored. The monochromatic luminosity [erg cm^{-2} s^{-1} Hz^{-1}] (Chen 2017) in the jet rest frame is

$$L_{\rm syn}(\nu) = \begin{cases} \frac{4}{3}\pi R^3\cdot 4\pi j_{\rm syn}(\nu)\cdot\left(1-\frac{3}{4}\tau\right) & \tau < 10^{-4}, \\ 2\pi^2R^3 j_{\rm syn}(\nu)\,\frac{2\tau^2-1+(2\tau+1)e^{-2\tau}}{\tau^3} & \text{else}. \end{cases} \tag{B5}$$

Therefore, the synchrotron radiation flux density [erg s^{-1}cm^{-2}Hz^{-1}] in the observer's reference frame is given by

$$F_{\rm syn,obs}(\nu_{\rm obs}) = \frac{L_{\rm syn}(\nu)}{4\pi d_{\rm L}^2}\delta^3(1+z), \tag{B6}$$

where $d_{\rm L}$ denotes the luminosity distance and the observed frequency is related to the source-frame frequency by $\nu_{\rm obs} = \nu\frac{\delta}{1+z}$.

B.3. *Synchrotron Self-Compton*

The SSC scattering power of a single electron moving in a seed radiation field is

$$P_{\rm ssc}(\nu,\gamma) = 3\sigma_{\rm T}{\rm hc}\int f(\gamma,\nu_i,\nu_{\rm s})\,n_{\rm ph}(\nu_i)\,d\nu_i, \tag{B7}$$

where $\nu_{\rm i}$ and $\nu_{\rm s}$ are incident photon frequencies and scattered photon frequencies, respectively, and $\nu_{\rm i} \in [\frac{\nu_{\rm s}}{4\gamma}, \frac{3m_ec^2}{4h\gamma}]$. For the SSC process, the target photons required for inverse Compton scattering are provided by the synchrotron radiation itself, and the number density of the corresponding seed photon field is given by

$$n_{\rm ph} = \frac{9L_{\rm syn}}{16\pi R^2 c}\frac{1}{h\nu}. \tag{B8}$$

The inverse Compton scattering core function (Jones 1968; Blumenthal & Gould 1970) expressed as

$$f(\gamma, \nu_i, \nu_s) = \begin{cases} x\left(2x\ln x + 1 + x - 2x^2\right) & 0 < x < 1, \\ 0 & \text{else}, \end{cases} \tag{B9}$$

where $x \equiv \nu_s/(4\gamma^2\nu_i)$. The SSC emissivity [erg s^{-1} cm^{-3} Hz^{-1} sr^{-1}], which arises from a large population of electrons, is given by

$$j_{\rm ssc}(\nu) = \frac{1}{4\pi}\int P_{\rm ssc}(\nu,\gamma)N(\gamma)d\gamma. \tag{B10}$$

In addition, the approximation method for Klein-Nishina (KN) effect in Ghisellini et al. (1998) is applied to the SSC process,

$$\sigma_{\rm KN} = \begin{cases} \sigma_{\rm T} & \gamma\,\varepsilon \leqslant 3/4, \\ 0 & \text{else}, \end{cases} \tag{B11}$$

where ε is the dimensionless energy of the seed photon in units of $m_e c^2$. Finally, the monochromatic SSC luminosity [erg s^{-1} Hz^{-1}] in the jet rest frame is given by

$$L_{\rm ssc} = \frac{16}{3}\pi^2 R^3 j_{\rm ssc}(\nu). \tag{B12}$$

Therefore, the SSC radiation flux density [erg s^{-1}cm^{-2} Hz^{-1}] in the observer's reference frame is given by

$$F_{\rm ssc,obs}(\nu_{\rm obs}) = \frac{L_{\rm ssc}(\nu)}{4\pi d_{\rm L}^2}\delta^3(1+z). \tag{B13}$$

B.4. *Attenuated γ-rays by Pair Production.*

The γ-rays produced in the jet would be attenuated due to pair production ($\gamma\gamma \to {\rm e}^+{\rm e}^-$) interactions with synchrotron pthones, the total cross-section (Aharonian 2004) is given by

$$\begin{aligned}\sigma_{\gamma\gamma}(\nu,\nu_{\rm i}) = \frac{3\sigma_{\rm T}}{2s^2}\Bigg[&\left(s + \frac{1}{2}\ln s - \frac{1}{6} + \frac{1}{2s}\right)\ln(\sqrt{s}+\sqrt{s-1}) \\ &- \left(s + \frac{4}{9} - \frac{1}{9s}\right)\sqrt{1-\frac{1}{s}}\Bigg],\end{aligned} \tag{B14}$$

where $s \equiv h^2\nu\nu_{\rm i}/m_{\rm e}^2c^4$, $h\nu$ is the energy of the γ-rays and $h\nu_{\rm i}$ is the energy of the incident target photon. $\sigma_{\gamma\gamma}(\nu,\nu_{\rm i})$ reaches its maximum value $\sim 0.22\sigma_{\rm T}$ at $s = 3.5$. The optical depth to pair production (Liu et al. 2025) is given by

$$\tau_{\gamma\gamma}(\nu) = \int_{\nu_{\rm min}}^{\nu_{\rm max}} n_{\rm ph}(\nu_{\rm i})\,\sigma_{\gamma\gamma}(\nu,\nu_{\rm i})\,R\,{\rm d}\nu_{\rm i}. \tag{B15}$$

In the uniformity assumption of non-thermal electrons, the γ-ray photons remaining after attenuation are given by attenuation factor (Dermer & Menon 2009)

$$A_{\rm syn} = \frac{3}{\tau_{\gamma\gamma}(\nu)}\left\{\frac{1}{2} + \frac{\exp\left[-\tau_{\gamma\gamma}(\nu)\right]}{\tau_{\gamma\gamma}(\nu)} - \frac{1-\exp\left[-\tau_{\gamma\gamma}(\nu)\right]}{\tau_{\gamma\gamma}(\nu)^2}\right\}. \tag{B16}$$

On the other hand, TeV γ-photons from the source are attenuated by photons of the EBL photons due to pair production. EBL absorption optical depth $\tau_{\rm EBL}$ is given by Finke et al. (2022), and attenuation factor (Xue et al. 2022) is given by

$$A_{\rm EBL} = e^{-\tau_{\rm EBL}}. \tag{B17}$$

Finally, the observed flux [erg cm^{-2} s^{-1}] is expressed as

$$F'_{\rm ssc,obs} = \nu_{\rm obs}F_{\rm ssc,obs}A_{\rm syn}A_{\rm EBL}. \tag{B18}$$